UNIVERSIDADE ESTADUAL DE MARINGÁ
CENTRO DE CIÊNCIAS BIOLÓGICAS
PROGRAMA DE PÓS-GRADUAÇÃO EM CIÊNCIAS BIOLÓGICAS
ÁREA DE CONCENTRAÇÃO EM BIOLOGIA CELULAR E MOLECULAR

JOSÉ RENATO PATTARO JÚNIOR

EXPRESSÃO E CARACTERIZAÇÃO BIOFÍSICA DE PROTEÍNAS ALVO DE FÁRMACOS: APLICAÇÕES NO DESCOBRIMENTO DE AGENTES ANTIMICROBIANOS

Maringá
2021

JOSÉ RENATO PATTARO JÚNIOR

EXPRESSÃO E CARACTERIZAÇÃO BIOFÍSICA DE PROTEÍNAS ALVO DE FÁRMACOS: APLICAÇÕES NO DESCOBRIMENTO DE AGENTES ANTIMICROBIANOS

Tese apresentada ao Programa de Pós-Graduação em Ciências Biológicas (área de concentração - Biologia Celular e Molecular), da Universidade Estadual de Maringá para a obtenção do grau de Doutor em Ciências Biológicas.

Orientador: Prof. Dr. Flávio A. V. Seixas
Coorientador: Prof. Dr. Quirino Alves de Lima Neto

Maringá
2021

JOSÉ RENATO PATTARO JÚNIOR

EXPRESSÃO E CARACTERIZAÇÃO BIOFÍSICA DE PROTEÍNAS ALVO DE FÁRMACOS: APLICAÇÕES NO DESCOBRIMENTO DE AGENTES ANTIMICROBIANOS

Tese apresentada ao Programa de Pós-Graduação em Ciências Biológicas (área de concentração - Biologia Celular e Molecular), da Universidade Estadual de Maringá para a obtenção do grau de Doutor em Ciências Biológicas.

Aprovado em: 30/09/2021

BANCA EXAMINADORA

_____
Prof. Dr. Flávio Augusto Vicente Seixas
Universidade Estadual de Maringá – UEM

_____
Profª. Dr. Fernanda Andréia Rosa
Universidade Estadual de Maringá – UEM

_____
Profª. Dra. Rosane Marina Peralta
Universidade Estadual de Maringá – UEM

_____
Profª. Dra. Fernanda Canduri
Universidade de São Paulo - USP

_____
Prof. Dr. Fernando Alves de Melo
Universidade Estadual Paulista - Unesp

BIOGRAFIA

José Renato Pattaro Júnior, filho de Leonice Aparecida Carmona Pattaro e José Renato Pattaro, nasceu no dia 11 de março de 1989 na cidade de Maringá, Paraná. Graduado em Bioquímica (Bacharelado) em 2014 pela Universidade Estadual de Maringá. Mestre pelo Programa de Pós-Graduação em Ciências Biológicas (área de concentração - Biologia Celular e Molecular), no qual realizou análises biofísicas e filogenéticas da proteína KIN humana expressa heterologamente em *E. coli*. Em março de 2017 iniciou o doutorado em Ciências Biológicas pelo mesmo programa, no qual finaliza o curso com a defesa da tese em 30 de setembro de 2021. Possui experiência na área de Biologia Celular e Bioquímica Molecular, atuando principalmente nos seguintes temas: tecnologias do DNA recombinante, biofísica, expressão heteróloga de proteínas, sequenciamento de nova geração (NGS) e bioinformática.

"Dedico este modesto trabalho ao meu avô Antenor, um símbolo de fortaleza e resiliência implacável."

AGRADECIMENTOS

APRESENTAÇÃO

Esta tese de doutorado é composta de dois artigos completos de pesquisa original:

Biophysical characterization of recombinant *Escherichia coli* D-alanyl,D-alanine ligase B

José Renato Pattaro Júnior[a], Ícaro Putinhon Caruso[b,c], Jéssica Maróstica de Sá[b], Taniara Suelen Mezalira[a], Diego de Souza Lima[a], Eduardo Jorge Pilau[d], David Roper[e], Maria Aparecida Fernandez[f], Flavio Augusto Vicente Seixas[a]*

[a]Departament of Technology, Universidade Estadual de Maringá, Umuarama, PR, Brazil
[b]Department of Physics, Instituto de Biociências, Letras e Ciências Exatas – Universidade Estadual Paulista "Júlio de Mesquita Filho", São José do Rio Preto, SP, Brazil
[c]National Center for Nuclear Magnetic Resonance of Macromolecules, Institute of Medical Biochemistry and National Center for Structure Biology and Bioimaging (CENABIO), Universidade Federal do Rio de Janeiro, Ilha do Fundão, Rio de Janeiro, RJ, Brazil
[d]Departament of Chemistry, Universidade Estadual de Maringá, Maringá, PR, Brazil
[e]School of Life Sciences, The University of Warwick, Coventry, United Kingdom
[f]Departament of Biotechnology, Genetics and Cell Biology, Universidade Estadual de Maringá, Maringá, PR, Brazil

A ser submetido na revista *Biophysical Chemistry,* fator de impacto 2.352.

Atividade antiviral do extrato de *Poincianella pluviosa* contra SARS-CoV-2

José Renato Pattaro Júnior[1]; Ingrid Garcia Araújo[1]; Carolina Borsoi Moraes[3]; Gisele Strieder Philippsen[2]; Lucio Holanda Gondim de Freitas Junior[3]; João Carlos Pallazo de Mello[4]; Rosane Marina Peralta[5]; Maria Aparecida Fernandez[6]; Róbson Ricardo Teixeira[7]; Flavio Augusto Vicente Seixas[1]*

[1]Departamento de Tecnologia, Universidade Estadual de Maringá, Umuarama, PR, Brasil
[2]Universidade Federal do Paraná, Jandaia do Sul, PR, Brasil.
[3]Instituto de Ciências Biomédicas, Universidade de São Paulo, São Paulo, Brasil
[4]Departamento de Farmácia, Universidade Estadual de Maringá, Maringá, PR, Brasil
[5]Departamento de Bioquímica, Universidade Estadual de Maringá, Maringá, PR, Brasil
[6]Departamento de Biotecnologia, Genética e Biologia Celular, Universidade Estadual de Maringá, Maringá, PR, Brasil
[7]Departamento de Química, Universidade Federal de Viçosa, Viçosa, MG, Brasil

A ser submetido na revista *Clinical Biochemistry*, fator de impacto 3.281.

RESUMO GERAL

As doenças causadas por microrganismos acompanham a humanidade ao longo da história, tornando-se mais ameaçadoras quando a sociedade mudou do nomadismo para a vida agrária, há 10.000 anos. A evolução para comunidades mais conectadas resultou em condições propícias para o desenvolvimento de epidemias, sendo a gripe, varíola, malária, tuberculose e lepra doenças que assolaram a humanidade desde essa mudança. À medida que as comunidades se tornaram ainda mais conectadas, a probabilidade de pandemias aumentou, consequentemente. Atualmente, o uso indiscriminado de antibióticos e a elevada taxa de mutações de vírus de RNA (como o SARS-CoV-2) favoreceram a rápida evolução de cepas resistentes, o que acelerou a corrida por novas drogas com efeito antimicrobiano.

Considerando as emergentes preocupações sobre a resistência bacteriana aos antibióticos existentes e a iminência do surgimento de uma cepa viral que seja resistente parcial ou integralmente às vacinas atuais, os dois estudos apresentados, tiveram os objetivos de: (**1**) realizar a caracterização biofísica de DdlB de *Escherichia coli* recombinante (*Ec*DdlB), quanto aos parâmetros de temperatura de *melting* (T_m), entalpia de desnaturação calorimétrica e de van't Hoff (ΔH_{cal}^{U} and ΔH_{vH}^{U}), bem como a caracterização de elementos de estrutura secundária em três pHs diferentes, a fim de avaliar as variações no padrão de dobramento/desdobramento em função do pH e da temperatura. (**2**) Prospectar novos compostos inibidores de M^{pro} de SARS-CoV-2 em extratos de *Poincianella pluviosa* (Sibipiruna) e compostos sintéticos, a partir de varredura virtual (*in silico*), e avaliar seu potencial inibitório em ensaios proteolíticos com M^{pro} recombinante e ensaios com células Vero E6 infectadas.

A proteína *Ec*DdlB, expressa heterologamente, foi empregada em testes de atividade enzimática acoplada à piruvato quinase (PK)/lactato desidrogenase (LDH), apresentando IC$_{50}$ de 10.5 ± 0.43 µM para a droga DCS (D-cicloserina), sendo compatível com a literatura. As deconvoluções dos espectros de dicroísmo circular (CD) a 20 ºC mostraram uma porcentagem majoritária de α-hélices nos pHs 5,4 e 9,4, enquanto em pH 7,4, uma contribuição igual de estruturas β e α-hélices foi calculada. As porcentagens de elementos de estrutura secundária *Ec*DdlB nos pHs de 5,4 e 9,4 corroboram as estatísticas da estrutura cristalográfica, PDB ID: 4C5C, obtida em um pH de 8,0. Essa diferença nas porcentagens entre as estruturas secundárias do modelo cristalográfico e de DdlB em pH

7,4 pode ter sido causada por dois motivos: 1) pela existência de um grupo cromofórico ligado apenas em 7,4, o que induz um viés na medição ou 2) pela modificação da estrutura proteica no modelo, causada pela utilização de PEG 6000 no tampão de cristalização.

Nos ensaios de desnaturação térmica, a estabilidade de *Ec*DdlB aumentou com a proximidade de seu ponto isoelétrico teórico (pI) de 5,0, atingindo o máximo no pH 5,4, com T_m de 52,68 ºC e ΔH_{vH}^{U} de 484 kJ·mol^{-1}. Um perfil incomum foi observado exclusivamente nos experimentos de desnaturação térmica em CD, representado por duas contribuições sigmoidais em pH 7,4, diferente do perfil cooperativo que tinha um único componente sigmoidal nos outros dois pHs testados. Isso pode ser explicado devido à influência do ATP ou ADP residuais ligados à DdlB. Os resultados obtidos de DCS (*Differential Scanning Calorimetry*) corroboraram com as desnaturações térmicas em CD, comprovando a irreversibilidade da desnaturação de *Ec*DdlB, com a conseguinte formação de agregados e aumento nas porcentagens de estruturas β, devido à formação de folhas-β intermoleculares.

No estudo com a proteína M^{pro} de SARS-CoV-2, ensaios de *docking* molecular *in silico* avaliaram a interação desta enzima com compostos presentes no extrato de *P. pluviosa* (fração acetato de etila – FAE e suas subfrações F4 e F2) e identificaram 4 compostos com melhor *score* do que o ligante referência X77 (*N-(4-tert-butylphenyl)-N-[(1R)-2-(cyclohexylamino)-2-oxo-1-(pyridin-3-yl)ethyl]-1H-imidazole-4-carboxamide*). As 3 frações e 4 compostos sintéticos foram avaliados nos testes cinéticos, com a proteína recombinante M^{pro} com substrato fluorogênico. O solvente DMSO, utilizado na dissolução dos compostos, apresentou atividade inibitória; assim, os testes foram normalizados em relação a uma amostra com a mesma concentração de DMSO contida nos testes com os extratos (Controle 2). O composto Pentagalloylglucose (PGG) apresentou o melhor resultado na inibição da atividade da M^{pro}, como previsto pelos experimentos *in silico*, com uma supressão da atividade em ~60%. Os compostos Bm6, Bm7 e Bm8 não apresentaram atividade inibitória nos ensaios *in vitro*; assim, não participaram dos testes em células infectadas.

Nos experimentos de citotoxicidade e atividade antiviral, realizados em células Vero E6 em cultura, todas as frações do extrato de *P. pluviosa* performaram melhor que o composto PGG isolado (66,44%), com as frações FAE e F2 alcançando inibição da atividade de M^{pro} em 100,5 e 101,83%, respectivamente, mesmo apresentando menor taxa

de sobrevivência celular. Contudo, diversos trabalhos com células em cultura e ensaios *in vivo*, disponíveis na literatura, demonstraram a baixa citotoxicidade dos extratos de Sibipiruna, em concentrações até maiores do que as utilizadas nos ensaios descritos neste trabalho. A proeminente atividade dos extratos, em células infectadas, pode ter sido ocasionada pelo efeito sinérgico de diversos polifenóis e taninos hidrolisáveis, constituintes em diversos alvos de SARS-CoV-2 e da célula hospedeira. As atividades antivirais dos extratos se mostraram bastante promissoras. Contudo, mais estudos são necessários, visando uma melhor compreensão da citotoxicidade, bem como a avaliação da aplicação do extrato de *P. pluviosa* contra a Covid-19 em estudos com modelos animais infectados.

Esperamos que os resultados apresentados nesta tese possam contribuir na geração de melhores modelos estruturais em experimentos de varredura virtual que buscam inibidores para a biossíntese de PG, bem como, no desenvolvimento de futuros novos inibidores frente à escassa terapêutica contra a Covid-19.

GENERAL ABSTRACT

Diseases caused by microorganisms have been following humanity throughout history, becoming even more threatening after society shifted from nomadism to agrarian life 10,000 years ago. The evolution towards more connected communities has resulted in favorable conditions for the development of epidemics, with flu, smallpox, malaria, tuberculosis and leprosy being diseases that have plagued humanity since its change. Also, the likelihood of pandemics increased accordingly. Moreover, the indiscriminate use of antibiotics and the high rate of RNA virus mutations (such as SARS-CoV-2) favored the rapid evolution of resistant strains, which has accelerated the race for new drugs with antimicrobial effect.

Considering the increasing concerns about bacterial resistance to existing antibiotics and the imminent emergence of a viral strain that might be partially or fully resistant to current vaccines, the two studies presented in this work aimed to: (**1**) perform the biophysical characterization of DdlB, from recombinant *Escherichia coli* (*Ec*DdlB), for parameters such as melting temperature (T_m), calorimetric denaturation enthalpy and van't Hoff (ΔH_{cal}^{U} and ΔH_{vH}^{U}), as well as characterization of secondary structure elements at three different pHs, in order to evaluate variations in the folding/unfolding pattern in function of pH and temperature, and, (**2**) prospect new SARS-CoV-2 M^{pro} inhibitor compounds in *Poincianella pluviosa* (Sibipiruna) extracts and synthetic compounds, from virtual scan (*in silico*), and evaluate its inhibitory potential in proteolytic assays with recombinant M^{pro} and infected Vero E6 cells.

The heterologously expressed *Ec*DdlB protein was used in enzymatic activity tests coupled to pyruvate kinase (PK)/lactate dehydrogenase (LDH), presenting an IC_{50} of 10.5 ± 0.43 µM for the DCS (D-cycloserine) drug, which is compatible with the literature. The deconvolutions of the circular dichroism (CD) spectra, at 20 ºC, showed a major percentage of α-helices at pH 5.4 and 9.4, while at pH 7.4, an equal contribution of β-structures and α-helix was calculated. The percentages of *Ec*DdlB secondary structure elements, at pHs of 5.4 and 9.4, corroborate the statistics of the crystallographic structure PDB ID: 4C5C, obtained at a pH of 8.0. This difference in the percentages between the secondary structures of the crystallographic model and DdlB, at pH 7.4, may have been caused by two reasons: 1) the existence of a chromophoric group linked only at 7.4, which

leads to a measurement bias or 2) by the modification of the protein structure in the model, caused using PEG 6000 in the crystallization buffer.

In thermal denaturation tests, the stability of *Ec*DdlB increased closer to its theoretical isoelectric point (pI) of 5.0, reaching a maximum at pH 5.4, with a T_m of 52.68 °C and ΔH_{vH}^{U} of 484 kJ.mol^{-1}. An unusual profile was observed exclusively in the thermal denaturation experiments in CD, represented by two sigmoidal contributions at pH 7.4, different from the cooperative profile, which had a single sigmoidal component at the other two tested pHs. This can be explained due to the influence of residual ATP or ADP linked to DdlB. The results obtained from DCS (Differential Scanning Calorimetry) corroborated with the thermal denaturations in CD, proving the irreversibility of *Ec*DdlB denaturation, with the consequent formation of aggregates and increase in the percentages of β-structures, due to the formation of intermolecular β-sheets.

In the study with the M^{pro} protein of SARS-CoV-2, *in silico* molecular docking assays evaluated the interaction of this enzyme with compounds present in the extract of *P. pluviosa* (ethyl acetate fraction – FAE and its subfractions F4 and F2) and identified 4 compounds with better score than the reference ligand X77 (N-(4-tert-butylphenyl)-N-[(1R)-2-(cyclohexylamino)-2-oxo-1-(pyridin-3-yl)ethyl]-1H-imidazole-4-carboxamide). The 3 fractions and 4 synthetic compounds were evaluated in kinetic tests, with the recombinant M^{pro} protein and fluorogenic substrate. The DMSO solvent, used in dissolution of compounds, showed inhibitory activity. Thus, tests were normalized in relation to a sample with the same DMSO concentration, contained in the tests with the extracts (Control 2). Compound Pentagalloylglucose (PGG) showed the best result in inhibiting the activity of M^{pro}, as predicted by *in silico* experiments, with an activity suppression of ~60%. The compounds Bm6, Bm7 and Bm8 did not show inhibitory activity in *in vitro* assays, Thus, they did not participate in the tests on infected cells.

Cytotoxicity and antiviral activity experiments were performed on cultured Vero E6 cells. All fractions of *P. pluviosa* extract produced better results than the isolated PGG compound (66.44%), with the FAE and F2 fractions achieving 100.5 and 101.83%, respectively, of M^{pro} activity inhibition. However, they presented lower cell survival rates. It is important to notice that several studies, with cellular cultures and *in vivo* assays, available in the literature, demonstrated low cytotoxicity of Sibipiruna extracts at concentrations even higher than those used in the assays described in this work. The

prominent activity of the extracts, in infected cells, may have been caused by the synergistic effect of different constituent polyphenols and hydrolysable tannins in various SARS-CoV-2 and host cell targets. The antiviral activities of the extracts are very promising. More specialized studies are required, in order to better understand the cytotoxicity, as well as the evaluation of the application of *P. pluviosa* extracts against Covid-19 with infected animal models.

We hope that the results presented in this thesis can contribute to the generation of better structural models for virtual scanning experiments that look for inhibitors for PG biosynthesis, as well as to the development of new inhibitors, in face of the scarce therapeutics strategies against Covid-19.

Sumário

Biophysical characterization of recombinant *Escherichia coli* D-alanyl,D-alanine ligase B

José Renato Pattaro Júnior[a], Ícaro Putinhon Caruso[b,c], Jéssica Maróstica de Sá[b], Taniara Suelen Mezalira[a], Diego de Souza Lima[a], Eduardo Jorge Pilau[d], David Roper[e], Maria Aparecida Fernandez[f], Flavio Augusto Vicente Seixas[a*]

[a]Departament of Technology, Universidade Estadual de Maringá, Umuarama, PR, Brazil
[b]Department of Physics, Instituto de Biociências, Letras e Ciências Exatas – Universidade Estadual Paulista "Júlio de Mesquita Filho", São José do Rio Preto, SP, Brazil
[c]National Center for Nuclear Magnetic Resonance of Macromolecules, Institute of Medical Biochemistry and National Center for Structure Biology and Bioimaging (CENABIO), Universidade Federal do Rio de Janeiro, Ilha do Fundão, Rio de Janeiro, RJ, Brazil
[d]Departament of Chemistry, Universidade Estadual de Maringá, Maringá, PR, Brazil
[e]School of Life Sciences, The University of Warwick, Coventry, United Kingdom
[f]Departament of Biotechnology, Genetics and Cell Biology, Universidade Estadual de Maringá, Maringá, PR, Brazil

*Corresponding Author
Dr. Flávio A. V. Seixas
Av. Ângelo Moreira da Fonseca, 1800, Jd Universitário
87506-370, Umuarama, PR, Brazil
+55 44 3621 9337
favseixas@uem.br

List of Abbreviations

AR - Alanine Racemase

CD - Circular Dichroism

CS - Concentrated Fraction

D-Ala – D-alanine

D-Ala,D-Ala or DalDal – D-alanyl,D-alanine

DCS - D-cycloserine

DdlB - D-alanyl,D-alanine ligase

DLS - Dynamic Light Scattering

DSC - Differential Scanning Calorimetry

FTIR - Fourier Transform Infrared

GlcNAc - N-acetylglucosamine

HT - HisTrap

iGlu – Isoglutamate

IPTG - Isopropyl β-D-1-thiogalactopyranoside

LB - Luria Bertani

LDH - Lactate Dehydrogenase

mDAP - Meso-diaminopimelic Acid

MurNAc - Acetylmuramic Acid

MW - Molecular Weight

NMR - Nuclear Magnetic Resonance

PDB ID – Protein Data Bank Identity

PEG - Polyethylene Glycol

PEP - Phosphoenolpyruvate

pI – Isoelectric Point

PIX - Positional Isotope Exchange Technique

PK - Pyruvate Kinase

PMF - Peptide Mass Fingerprinting

T_m - melting temperature

ABSTRACT

Peptidoglycan (PG) is a key structural component of the bacterial cell wall and interruption of its biosynthesis is a validated target for antimicrobials. Of the enzymes involved in PG biosynthesis, D-alanyl,D-alanine ligase B (DdlB), is responsible for the condensation of two alanines, forming D-Ala-D-Ala, which is required for subsequent extracellular transpeptidase crosslinking of the mature peptidoglycan polymer. In this work, we aimed the biophysical characterization of recombinant *Escherichia coli* DdlB (*Ec*DdlB), regarding parameters of melting temperature (*Tm*), calorimetry and van't Hoff enthalpy changes of denaturation (ΔH_{cal}^{U} and ΔH_{vH}^{U}), as well as characterization of elements of secondary structure at three different pHs. These are essential parameters to include in virtual screening efforts to find new inhibitors to DdlB. The stability of *Ec*DdlB increased with proximity to its pI of 5.0, reaching the maximum at pH 5.4 with T_m and ΔH_{vH}^{U} of 52.68 ℃ and 484 kJ·mol^{-1}, respectively. An unusual profile was observed exclusively in the circular dichroism (CD) thermal denaturation experiments, represented by two sigmoidal contributions at pH 7.4, different from the cooperative profile that had a single sigmoidal component at other pHs. This may be explained by the influence of residual ATP or ADP bonded to DdlB. Deconvolutions of the CD spectra at 20 ℃ showed a majority percentage of α-helix at pH 5.4 and 9.4, whereas for pH 7.4, an equal contribution of β-structures and α-helices was calculated. Thermal denaturation process of *Ec*DdlB proved to be irreversible with an increase in β-structures that can contribute to the formation of protein aggregates.

1. Introduction

The indiscriminate use of antibiotics has been rapidly accompanied by the emergence of resistant strains, where bacteria are probably the most important agents in terms of morbidity and mortality [1]. In the search for new antibiotics, the peptidoglycan biosynthesis process has been one of the targets that has received the most attention. Peptidoglycan (PG) is the key structural component found exclusively in the bacterial cell wall, being responsible for providing form and rigidity to this structure, maintaining cell viability, and resistance to internal turgor pressure [2]. It is basically composed of linear polymeric chains of disaccharide un its of N-acetylglucosamine (GlcNAc) β(1→4) N-acetylmuramic acid (MurNAc) linked by crossed pentapeptide chains, whose composition is diverse, with variations being species-specific [3]. In *Escherichia coli*, the pentapeptide in the growing PG consists of L-Ala-D-iGlu-mDAP-D-Ala-D-Ala (iGlu: isoglutamate and mDAP: meso-diaminopimelic acid), where the most frequent cross-link is the amide bond between D-Ala and mDAP of two adjacent peptides. Enzymes that promote PG cross-linking use the D-Ala,D-Ala peptide as a universal substrate [4]. Due to the fact that D-amino acids are characteristic of bacterial PG, together with their biosynthetic machinery, it becomes an interesting target for the development of new drugs.

Thus, the enzyme D-alanyl,D-alanine ligase (Ddl), also known as D-alanyl,D-alanine synthetase (EC: 6.3.2.4), emerges as a promising target for drug development, since the inhibition of this enzyme has a lethal effect on prokaryotic microorganisms that are D-alanine dependent [5]. Ddl catalyzes the condensation between two D-Ala to form the D-Alanyl,D-Alanine dipeptide (DalDal) with the consumption of an ATP (reaction 1) [6]. One D-Ala produced by the enzyme alanine racemase (AR) docks to the D-Ala$_1$ site with high affinity, and subsequent phosphorylation of D-alanine occurs in the carboxyl group by ATP γ-phosphate (distinct and exclusive binding site for ATP), producing an acyl-phosphate intermediate [7,8]. After the docking of the second D-Ala (D-Ala$_2$ site), condensation is completed with a nucleophilic attack by the D-Ala amine group of the D-Ala$_2$ site to the phosphorylated D-Ala of the D-Ala$_1$ site, producing DalDal) [8,9]. Then, the D-Ala,D-Ala-adding enzyme binds DalDal to the terminal portion of UDP-muramyl tripeptide to form a product with a DalDal N-acylated terminal, which is the unit UDP-Mur-Nac pentapeptide precursor of the bacterial cell wall [7].

$$2\,DAla + ATP \xrightarrow[\text{DdlB}]{Mg^{2+}} DAla, DAla + ADP + Pi \qquad (1)$$
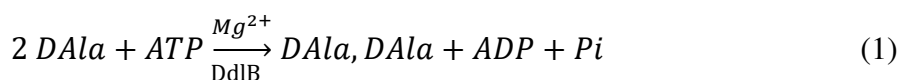
Although few, Ddl inhibitors have already been reported [10–12], including D-cycloserine (DCS), a D-ala mimic that competitively inhibits Ddl [13]. However, its use is limited due to significant adverse effects, such as seizures and peripheral neuropathy [14]. The enzyme alanine racemase (AR) is also inhibited by DCS, interrupting the supply of the substrate for Ddl. However, resistant strains of *Mycobacterium smegmatis* bypassed this inhibitory effect by overexpression of DCS target proteins, but it is not clear whether AR, Ddl, or both have increased expression [15]. DCS is the only Ddl inhibitor currently used against bacterial infections and has been applied more often as an anti-tuberculosis agent [16,17].

Although the 3D structure of Ddl isoforms A and B have already been solved by X-ray crystallography [11–13,18], which can be used to prospect for new inhibitors by structure based screening assays, the lack of structural information regarding proteins in solution under different conditions makes the development of new drugs a greater challenge [19–21]. In this context, recent work has proven the successful strategy of combining virtual screening with several complementary and synergistic biophysical methods in the development of new ligands [22].

Given the above, this work aimed to perform biophysical characterization of the recombinant D-alanyl,D-alanine ligase B from *Escherichia coli* (*Ec*DdlB) - EC 6.3.2.4, regarding the parameters of melting temperature (*Tm*), enthalpies of denaturation (ΔH_{cal}^{U} and ΔH_{vH}^{U}), and characterization of secondary structure elements under three different pH conditions for the first time. In addition, we aimed to contribute to the expansion of DdlB informational data, such as biophysical parameters with knowledge on variations in the folding/unfolding pattern as a function of pH and temperature. Therefore, important information about the structural stability of this protein in different physiological conditions could be provided. Thus, the use of this data in association with the 3D structure of *Ec*DdlB in structure based virtual screening simulations, may contribute to the development of more effective inhibitors in a way that will increase the small number of inhibitors of this important drug target.

2. Material and methods

2.1. Expression, purification, and identification of the EcDdlB protein by LC-MS^{E}

Strains of *E. coli* BL21 (DE3) were transformed with the plasmid pProEX::*Ec*DdlB [23], kindly provided by Dr. David Roper (University of Warwick, UK). Bacteria were cultured aerobically in LB (Luria Bertani) medium plus 50 µg·mL^{-1} ampicillin at 37 ℃. After the culture reached an OD_{600} of 0.6, overexpression of amino terminally histidine-tagged DdlB was induced using IPTG (Isopropyl β-D-1-thiogalactopyranoside) at a final concentration of 1 mM. After 4 h of induction at 37 ℃, the culture was centrifuged at 10,000 × g for 10 min at 4 ℃ and the pellet was washed with 20 mM Tris-HCl (pH 8.0) and stored at -20 ℃ for 12–16 hours before extraction.

The pellet was resuspended in lysis buffer (50 mM NaH_2PO_4, 300 mM NaCl, and 10 mM Imidazole, pH 7.4 with 1× protease inhibitor) and sonicated on ice for 4 min with pulses of 20 s on and 20 s off with an amplitude of 60% in a Fisher Scientific sonicator. Cell debris was eliminated by centrifugation at 15,000 × g for 10 min at 4 ℃ and the supernatant was filtered through a 0.22 µm Millex$^{®}$ syringe filter (Merck-Millipore, GER) to separate the fraction of soluble proteins. Subsequently, the supernatant was applied to a 1 mL nickel-sepharose column (HisTrap, GE) using Fast Protein Liquid Chromatography (FPLC; ÄKTA Pure, GE Lifesciences, Sweden). The protein was eluted in a 10–300 mM imidazole gradient.

The molecular weight of *Ec*DdlB under non-denaturing conditions was calculated using the gel filtration method, through a Superdex 200 10/300 column passage (GE Lifesciences) coupled to an FPLC Äkta Pure (GE Lifesciences, Sweden). The calibration curve was constructed using the LMW and HMW gel filtration calibration kit (GE Lifesciences), following the manufacturer's recommendations. The proteins were eluted in isocratic mode with 50 mM Phosphate buffer + 150 mM NaCl (pH 7.2) at room temperature and a flow rate of 0.5 mL·min^{-1}. Absorbances were monitored at 214 and 280 nm. The elution volumes for each protein were measured and converted to K_{av} (equation 1) and plotted against the logarithm of the respective molecular weights (*log*MW),

$$K_{av} = \frac{V_e - V_o}{V_c - V_o} \tag{1}$$

where V_e = elution volume, V_o = column void volume, and V_c = geometric column volume.

The proteins had their buffers changed for the biophysical and kinetics assays by 4 HiTrap Desalting (GE) columns of 5 mL coupled in tandem. The samples were concentrated using Amicon® centrifuge filters with a 10 kDa cut off (Merck-Millipore) and quantified at 280 nm, using a molar extinction coefficient of 1.226 L·g^{-1}·cm^{-1} for converting Abs to mg·mL^{-1} estimated by ProtParam [24]. Analysis of the purification and concentration of the samples was performed by 12% SDS-PAGE.

The samples were prepared for mass spectrometry following the standard protocol [25], modified and adapted by National Biosciences Laboratory [26]. Analysis of the triptych peptides was performed in an M-Class Waters nanoLC coupled to a Waters Xexo G2-si mass spectrometer (Q-TOF geometry), using acquisition mode MS^{E}. After analysis, the RAW files were processed using ProteinLynx Global Server version 3.0.3 (Waters) with a database for *Escherichia coli* proteins from Uniprot.

2.2. Enzyme activity assays

The kinetic experiments using *Ec*DdlB were performed according to the enzyme activity assay coupled to pyruvate kinase (PK) / lactate dehydrogenase (LDH) [27], where initial velocities (60 s) were evaluated in a UV-visible UV-165PC spectrophotometer (Shimadzu, Japan), couplet with a thermostatic bath at 25 ºC. The assay solution had the following components: 100 mM HEPES (pH 7.8), 10 mM KCl, 10 mM $MgCl_2$, 5 mM ATP, 2.5 mM phosphoenolpyruvate (PEP), 0.1 mM NADH, 50 µg·mL^{-1} lactate dehydrogenase (LDH), 0.14 mg·mL^{-1} PK, *Ec*DdlB (22 nM), and D-alanine (0.4–8.0 mM). The change in absorbance caused by consumption of NADH was monitored at 340 nm. The inhibitor D-cycloserine (Sigma-Aldrich) was used as a positive control for the validation of the expressed protein. The velocities were adjusted to the Michaelis-Menten equation (Equation 2).

$$V = \frac{Vmax.[S]}{Km+[S]} \tag{2}$$

where *V* is the velocity at substrate concentration *S*, V_{max} is the maximum velocity, and K_m is the Michaelis constant. In DCS assays, the D-alanine concentration was maintained at 0.4 mM and the inhibitor concentration ranged from 0.025 to 50 µM. The velocities were adjusted using Equation 3 to obtain the IC$_{50}$ value.

$$y = \frac{A1 - A2}{1 + exp^{(x-x0)/dx}} + A2 \qquad (3)$$

2.3. Circular dichroism

Circular dichroism (CD) experiments were performed in a Jasco J-815 spectropolarimeter (Jasco, USA) equipped with a Peltier system for temperature control, using a 1.0 mm optical path quartz cuvette. The CD-UV far spectra of the enzyme were collected in the range of 260–190 nm with a scanning speed of 50 nm·min^{-1}, response time of 1.0 s, spectral bandwidth of 1.0 nm, spectral resolution of 0.2 nm, and 10 accumulations. Measurements of circular dichroism using the enzyme EcDdlB were acquired at a pH of 5.4, 7.4, and 9.4 and temperatures of 20 and 90 °C for each pH. The protein was diluted to 3.5 μM in phosphate-citrate buffer (20 mM Na_2HPO_4, 50 mM NaF, pH 5.4), mono-dibasic sodium phosphate (20 mM Na_2HPO_4/NaH_2PO_4, 50 mM NaF, pH 7.4), and glycine-hydrochloric acid (20 mM $C_2H_5NO_2$, 50 mM NaF, pH 9.4). The contributions of the buffer spectra were subtracted from the EcDdlB CD spectrum. Then, the resulting CD spectra were recorded as millidegrees (θ), and their values were converted into molar ellipticity ([Θ], deg·cm^2·dmol^{-1}) by Equation 4:

$$[\Theta] = \frac{\theta(m\ deg)}{10[P]\ l\ Nr} \qquad (4)$$

where [P] is the molar concentration of protein (3.5 μM), Nr is the number of amino acid residues (306), and l is the cuvette light path (cm). The percentage of secondary structures was estimated from the CONTINLL algorithm by means of the CDPro program package, using the SMP56 protein reference set (reference set of 56 soluble + membrane proteins) [28].

DdlB thermal denaturation experiments (3.5 μM) were performed in the same spectropolarimeter in which the measurements of the CD-UV far spectral profile were performed, using the same 1.0 mm quartz cuvette. Thermal unfolding was carried out from 20 to 90 ℃ at a heating rate of 1.0 °C·min^{-1}, with measurements being performed every 2 ℃, and at the same pH levels as the spectral profiles of the enzyme. The collected spectral range was 223 to 199 nm, with a scanning speed of 50 nm·min^{-1}, response time of 1.0 s, spectral bandwidth of 1.0 nm, spectral resolution of 0.2 nm, and 3 accumulations. The fraction of denatured enzyme was determined by Equation 5,

$$f_U = \frac{\theta - \theta u}{\theta n - \theta u} \tag{5}$$

where θ is the sign from the circular dichroism of the enzyme at each investigated temperature, θn, and θu are signs from the first (native) and last (denatured) temperature analyzed, respectively. Therefore, the fraction of native enzyme can be calculated by $f_N = f_U - 1$.

The temperature, where $f_N = f_U$, is termed the thermal denaturation temperature (T_m). Using a two-state transition model (native $\leftrightarrow$ unfolded) for thermal denaturation of the protein and calculating the equilibrium constant of this process as $K_{eq}^{U} = f_U / f_N$, van't Hoff's enthalpy variation for the denaturation process (ΔH_{vH}^{U}) was determined by the following equation:

$$\frac{d}{d^1/_T} \ln K_{eq}^{U} = \frac{\Delta H_{vH}^{U}}{R} \tag{6}$$

2.4. Differential scanning calorimetry (DSC)

DSC experiments were performed using the N-DSC III calorimeter (TA Instruments, USA) in the temperature range from 10 to 90 °C with heating and cooling scanning rates of 0.5 and 1.0 °C·min^{-1}. For DSC measurements, the protein was diluted in mono-dibasic sodium phosphate buffer (20 mM Na$_2$HPO$_4$/NaH$_2$PO$_4$, 50 mM NaF) at a pH of 7.4 for concentrations of 0.5 and 1.0 mg·mL^{-1}. The calorimetric cells were filled with the buffer solution equilibrated at 10 °C for 10 min and examined repeatedly at the interval of 10–90 °C until the baseline was reproducible. After calibrating the baseline with the buffer solution, the sample cell of the calorimeter had its' solution replaced by another containing the enzyme DdlB. The temperature scanning process with the equipment containing the enzyme occurred from a heating and cooling range of 10 to 90 °C to perform the enzyme denaturation process and investigate thermal refolding. The contribution of heat capacity at a constant pressure (C_P, kJ·mol^{-1}·K^{-1}) of the buffer solution was subtracted from the DdlB C_P values in the investigated temperature range.

The ΔH_{vH}^{U} value for the DdlB thermal unfolding process was determined by the van't Hoff ratio ($\ln K_{eq}^{U}$ & $1/T$) as described by CD measurements (section 2.3), being the fraction of denatured enzyme (f_U) calculated by a discretized thermogram integration process. The variation in calorimetric enthalpy (ΔH_{cal}^{U}) for the denaturation process was determined by calculating the area of the protein thermogram, after the baseline had been corrected.

2.5. Thermal denaturation of DD1B by fluorescence spectroscopy

Fluorescence spectroscopy experiments were performed on ISS PC1 - Photon Counting Spectrofluorimeter equipment (Champaign, IL, USA) coupled with a Neslab RTE-221 thermal bath. The excitation and emission slits were 8 nm wide and samples were analyzed in a 1.0 cm quartz cuvette. An excitation wavelength of 295 nm was chosen since it exclusively selects DdlB tryptophan residues. The enzyme was diluted in mono-dibasic sodium phosphate buffer at a pH of 7.4 to a concentration of 3.5 μM (20 mM NaH$_2$PO$_4$/Na$_2$HPO$_4$, 50 mM NaF). The emission spectra of the enzyme were collected in the spectral range from 305 to 500 nm and then corrected for the contribution of the fluorescence spectrum of the buffer. The protein denaturation experiment was carried out from 20 to 90 °C with an increase of 2 °C per measurement. Equations 5 and 6 were used to treat and analyze the unfolding data, as well as in the CD and DSC analyses.

2.6. Dynamic light scattering

Dynamic light scattering (DLS) measurements were performed on Zetasizer Nano S90 equipment (Malvern, Panalytical, Netherlands and United Kingdom) equipped with temperature control and a 1.0 cm optical path with reduced volume (120 μL). DLS measurements were performed with a total of 30 scans, each acquired over 30 seconds. Determination of the hydrodynamic radius of the DdlB enzyme (2 mg·mL^{-1}) was performed at a pH of 7.4 (20 mM NaH$_2$PO$_4$/Na$_2$HPO$_4$, 50 mM NaF) at 20 °C. The protein sample was centrifuged at 27,000 × g for 15 min at 4 °C to eliminate non-soluble particles before measuring the molecular size.

3. Results

3.1. EcDdlB purification analysis by SDS-PAGE

After affinity chromatography purification, we estimated a good yield in the expression of *Ec*DdlB, being eluted an average of 3 mL at a concentration of ~0.6 mg·mL^{-1} for every 50 mL of cultured LB medium. The observed purity was also satisfactory, due to the appearance of only one band with a mass close to 34,533 Da, as predicted by Protparam, which corresponds to *Ec*DdlB with six histidine residues at its N-terminal. (*Ec*DdlB+His$_{6x}$).

Fig.1 shows the result of the purification steps after elution in a HisTrap (HT) column, buffer change by a HiTrap desalting column, and concentration. A very low amount of proteins passed through the 10 kDa filter during concentration by centrifugation. Buffer changes were necessary to prepare the protein in specific buffers for biophysical techniques (CD, DSC, fluorescence spectroscopy, and DLS) and kinetic assays. The sample present in the concentrated fraction (CS) was identified as DdlB from *E. coli* by means of peptide mass fingerprinting (PMF) analysis with 93% coverage of the amino acid sequence (Table S1, supplementary data).
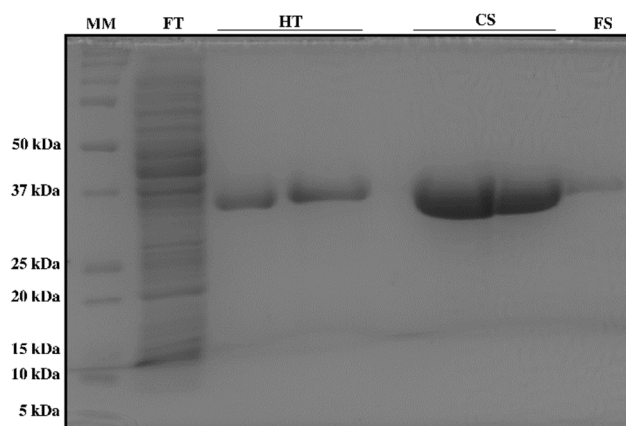
Fig. 1. SDS-PAGE (12%) showing the steps of purification and concentration of *Ec*DdDlB obtained on the LAS 500 equipment (GE). **MM** –Molecular Marker (Precision Plus Protein™ Dual Xtra Prestained Protein Standards, Bio Rad); **FT** - Flow Through; **HT –** HisTrap column eluted samples; **CS** – Samples concentrated in Amicon tubes of 10 kDa cutoff and, **FS -** Proteins that have passed through the Amicon filter. The concentrated samples were sufficiently pure to perform biophysical analyses.

The elution of *Ec*DdlB in a Superdex-200 10/300 column indicated that the protein had a molecular weight of ~66.2 kDa, a mass compatible with a homodimer in solution (Fig. 2). Hence, a ratio of 1.92 between the theoretical mass/column-eluted protein was found, confirming the dimeric state.
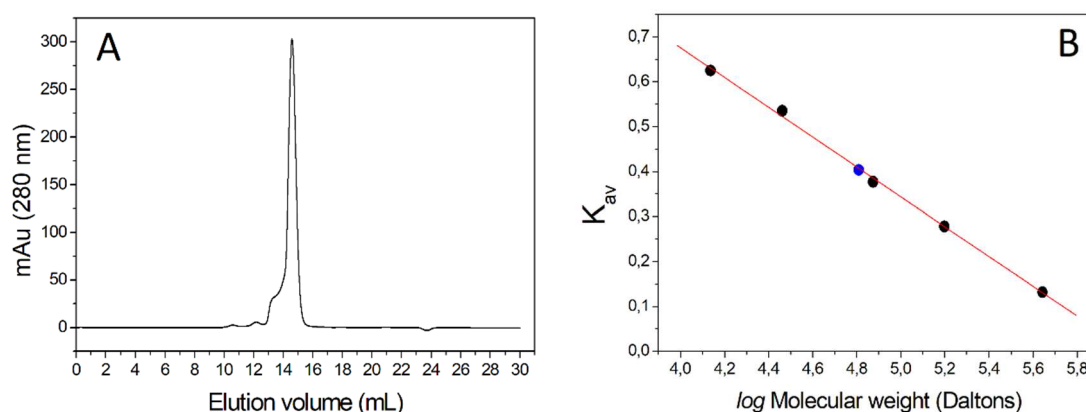
Fig. 2. (**A**) *Ec*DdlB elution chromatogram on a Superdex-200 10/300 column. (**B**) Plot showing the calibration dataset used to calculate the molecular weight of *Ec*DdlB. A protein mix (500 µL) of known molecular weights (black dots) was applied: Ferritin (440 kDa), Aldolase (158 kDa), Canalbumin (75 kDa), Carbonic anhydrase (29 kDa), and Ribonuclease (13.7 kDa). The elution volumes (black dots) and *Ec*DdlB (blue dot) were converted to K_{av} and plotted against log of their molecular weights. The MW of *Ec*DdlB was calculated by linear fit. Proteins were eluted in isocratic mode with 50 mM phosphate buffer + 150 mM NaCl at a pH of 7.2 and room temperature at a flow rate of 0.5 mL·min^{-1}. Absorbances were monitored at 214 and 280 nm. The estimated MW for *Ec*DdlB in solution was 66,203 Da, suggesting a homodimer as biological unity. Linear equation variables: a = 2.00381; b = −0.33196; K_{av} (y) = 0.40347; R = 0.99912.

3.2. EcDdlB catalytic activity assays

The catalytic activity of *Ec*DdlB was evaluated according to the substrate concentration at 25 ºC and a pH of 7.8. The adjustment of Equation 2 to data points in Fig. 3 provided a K_M value of 2.2 ± 0.6 mM and V_{max} of 355 ± 27 nM·min^{-1}. These values differ from those reported by Batson et al. (2017) for this enzyme, K_M = 167 ± 13 µM and V_{max} = 0.29 ± 0.01 µM.min^{-1}, which used the positional isotope exchange technique (PIX) with [γ-^{18}O$_4$]-ATP, where changes in the isotopic composition of the initial [γ^{18}O$_4$]-ATP species over time were monitored by ^{31}P NMR spectroscopy [12]. The PIX technique is more accurate than PK/LDH assay, it's because of the direct measurement of isotopically labeled phosphor atoms, without the need to couple other two enzymatic reactions.
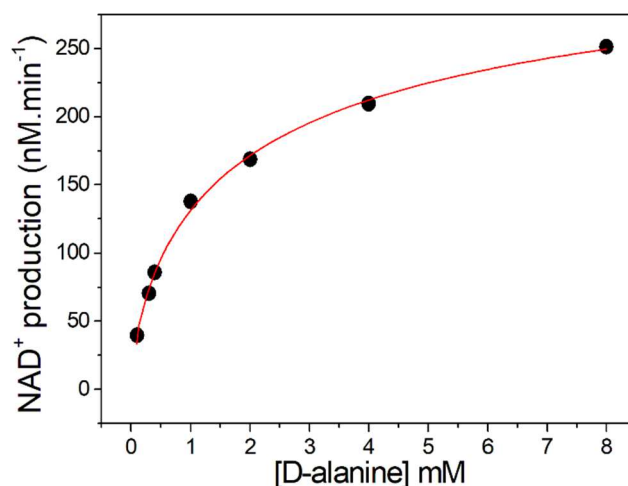
Fig. 3. *Ec*DdlB catalytic activity as a function of D-alanine substrate concentration. Experiment conditions: Hepes buffer 100 mM, pH 7.8, 10 mM KCl, 10 mM $MgCl_2$, 5 mM ATP, 2.5 mM PEP, 0.1 mM NADH, 50 µg·mL^{-1} lactate dehydrogenase (LDH), 0.14 mg·mL^{-1}, PK enzyme (0.63 µg), 25 ºC.

Analysis in the presence of the ligand D-cycloserine, a competitive inhibitor of D-Ala substrate [13], was performed as a way of further validation for the kinetic parameters of the expressed protein. The IC_{50} was 10.5 ± 0.4 µM (Fig. 4), a value very close to 11.5 ± 0.5 µM, which was previously found for this enzyme by Batson et al. (2017) [12]. The small difference found is due to the intrinsic precision of the two different techniques used.
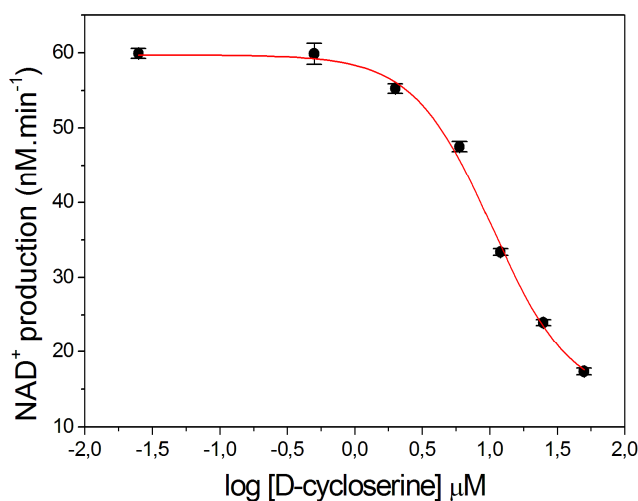
**Fig. 4.** Inhibition assays using the ligand D-cycloserine for evaluation of IC_{50}. The concentration of the substrate D-alanine was maintained at 0.4 mM and the concentration of D-cycloserine ranged from 0.025 to 50 µM. Equation 3 was adjusted to the experimental data points to obtain the IC_{50}.

3.3. Influence of pH on the characterization of secondary structure and thermal denaturation of DdlB determined by CD

The circular dichroism technique was used to estimate the secondary structure content of *Ec*DdlB under three different pH conditions: **1**) close to the theoretical pI of *Ec*DdlB (pH 5.4), **2**) near to the cytosolic pH of *E. coli* (pH 7.4) and **3**) an alkaline pH condition (pH 9.4). The CD-UV far spectra from *Ec*DdlB showed a similar profile at a pH of 5.4 and 9.4 at 293 K (20 °C) with a defined minimum of molar ellipticity at 208 nm together with a contribution around 222 nm and a positive ellipticity value above 200 nm (Fig. 5a). These spectral profile characteristics show the predominance of the secondary α-helix in the structural conformation of the enzyme. In contrast, the CD spectral profile of the protein at a pH of 7.4 showed a significant difference from those at a pH of 5.4 and 9.4, which suggests a decrease in the contribution of α-helix structural components (Fig. 5a).

To confirm the characteristics of the secondary structures of *Ec*DdlB, spectral deconvolutions of the CD data were performed at 20 °C at pH levels of 5.4, 7.4, and 9.4. Deconvolution results determined by the CONTINLL algorithm [28] revealed a majority percentage of α-helices for the enzyme at a pH of 5.4 and 9.4, whereas for a pH of 7.4, an equal contribution of β structures (β-strand/β-sheet) and α-helix was calculated (Table 1). The percentages of *Ec*DdlB secondary structure elements determined from the CD spectra at a pH of 5.4 and 9.4 corroborate the statistics from the crystallographic structure, PDB ID: 4C5C, obtained at a pH of 8.0 [12] and evaluated by the VADAR server [29], whereas at a pH of 7.4, there was no match between the CD and X-ray crystallography results.
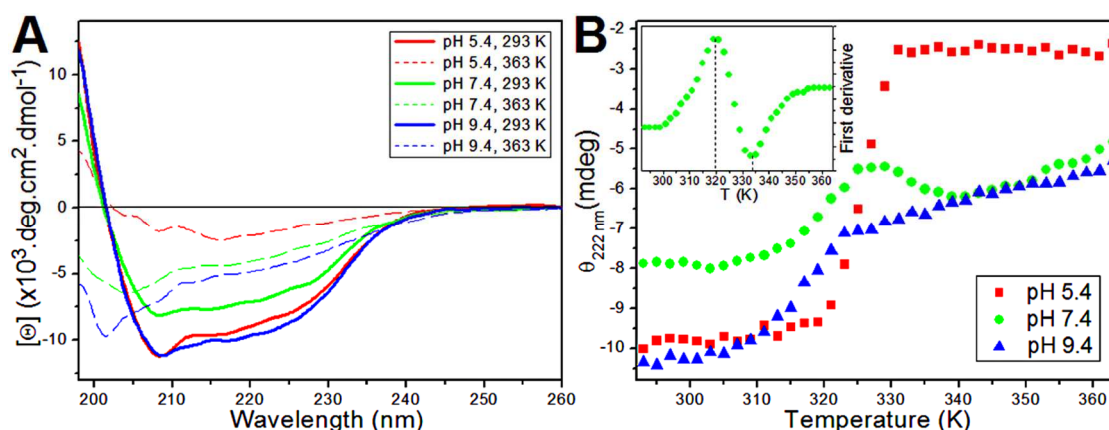
Fig. 5. (**A**) CD-UV far spectra from 3.5 μM *Ec*DdlB at a pH of 5.4, 7.4, and 9.4 and at temperatures of 293 (solid line) and 363 K (dashed line). (**B**) Values of molar ellipticity at 222 nm for the thermal denaturation process of the enzyme obtained between 293 and 363 K with a temperature increase of 2 K. The heating rate was 1.0 K·min^{-1}. The inset represents the first derivative of the unfolding curve at a pH of 7.4 and the dotted line marks the apparent transition points.

Table 1
Percentage of secondary structures of *Ec*DdlB under different pH and temperature conditions determined by the deconvolution of circular dichroism spectra, in comparison with the statistics of the crystallographic model PDB ID: 4C5C.

Secondary structure (%)	pH 5.4		pH 7.4		pH 9.4		4C5C
	293 K	363 K	292 K	363 K	293 K	363 K	crystal
α-helix	35	5	25	10	35	11	40
β-structure	18	45	26	36	18	32	19
Turn	18	21	20	23	19	25	10
Random coil	29	29	29	31	28	32	29

To characterize the thermal stability of *Ec*DdlB at a pH of 5.4, 7.4, and 9.4, thermal denaturation experiments were carried out using circular dichroism measurements in the temperature range from 293 (20 °C) to 363 K (90 °C). The CD spectra of the enzyme at 363 K (90 °C) at the investigated pH levels showed characteristics of an unfolded protein, with a disappearance of the minimum molar ellipticity at 208 and 222 nm and a decrease in positive ellipticity above 200 nm (Fig. 6a). The spectral deconvolution analysis revealed a significant reduction of α-helix secondary structures at all pH levels studied at 90 °C, plus an increase in β-structure content (Table 1).

The thermal denaturation profiles of the enzyme at pH levels of 5.4, 7.4, and 9.4 through the CD signal at 222 nm and as a function of temperature are shown in Fig. 5b. The temperature increases from 293 to 363 K at a pH of 5.4 and 9.4 showed a typically cooperative denaturation profile for the enzyme with a single sigmoidal component, whereas an unusual profile consisting of two sigmoidal contributions was observed for a pH of 7.4. Analysis of the normalized thermal denaturation curves of the enzyme for pH levels of 5.4 and 9.4 was performed based on a theoretical adjustment of Equations 5 and 6 to the experimental data (Fig. 6), considering a two-state model (see section 2.3). The thermal denaturation temperature (T_m) obtained was 325.6 ± 0.1 (52.68 °C) and 316.0 ± 0.2 K (43 °C) for the unfolding at pH levels of 5.4 and 9.4, while the change in van't Hoff enthalpy (ΔH_{vH}^{U}) was 484 ± 19 and 284 ± 15 kJ·mol⁻¹, respectively.
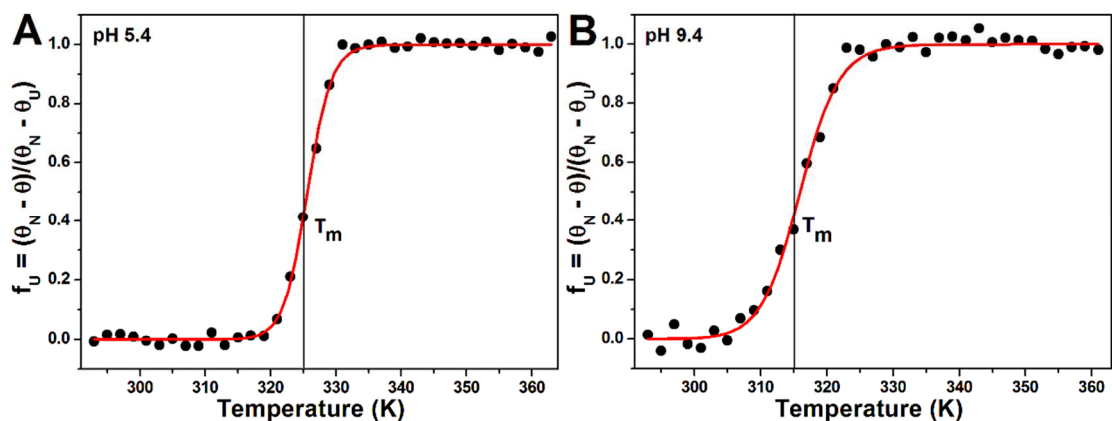
Fig. 6. Molar ellipticity, normalized at 222 nm, as a function of temperature for the thermal denaturation of *Ec*DdlB (3.5 μM) at (**A**) pH of 5.4 and (**B**) pH of 9.4. The filled circles represent the experimental data and the red line denotes the theoretical adjustment of Equations 5 and 6. The black line indicates the thermal denaturation temperature (T_m) of the protein.

Due to its anomalous and complex behavior, the thermal denaturation profile of *Ec*DdlB at a pH of 7.4 was not analyzed by the theoretical adjustment of Equations 5 and 6; however, the first derivative analysis revealed two apparent transition points referring to a minimum and maximum at 320.1 ± 0.1 (47.1 °C) and 332.9 ± 0.1 K (59.9 °C), respectively. The first apparent transition exhibited characteristics typical of thermal denaturation with a decrease in the magnitude of the CD signal and, therefore, must correspond to the main transition of the enzyme at a pH of 7.4. The second apparent transition could be understood as a particular and unusual chromophoric contribution, which in part would explain the discrepancy in quantification of the secondary structures of the enzyme at a pH of 7.4, determined by the spectral deconvolution regarding the crystalline structure of the protein. This behavior is uncommon and is an interesting fact about *Ec*DdlB.

To further investigate this phenomenon, another chromophoric probe was used; the intrinsic fluorescence of *Ec*DdlB tryptophans was also used to monitor the thermal denaturation of the enzyme at a pH of 7.4. Fig. 7a shows the emission spectra of the protein at 3.5 μM, in which suppression of fluorescence was observed with increasing temperature, characterizing the thermal unfolding of the enzyme. The T_m value obtained was 322.9 ± 0.5 K (49.9 °C) with a van't Hoff enthalpy variation of 243 ± 30 kJ·mol^{-1} (Fig. 7b), which were determined according to Equations 5 and 6 considering a two-state model. The melting temperature determined by the fluorescence technique was in accordance with the temperature value for the first apparent transition observed for the first derivative analysis of the CD data at a pH of 7.4.
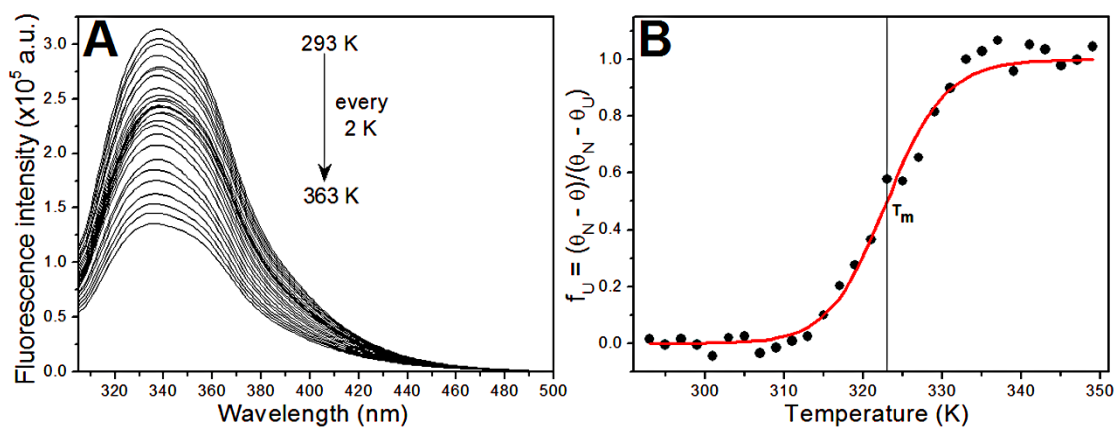
Fig. 7. (**A**) Fluorescence spectra of *Ec*DdlB (3.5 µM; pH 7.4) at different temperatures in the range from 293 to 363 K, with increments of 2 K. (**B**) Normalized thermal denaturation curve of the enzyme at the wavelength of 340 nm, which corresponds to the maximum fluorescence emission. The filled circles represent the experimental data and the red line denotes the theoretical adjustment of Equations 5 and 6. The black line indicates the thermal denaturation temperature (T_m) of the protein.

The pH variation of the DdlB buffer solution has made significant changes in the values of the thermodynamic parameters determined for the process of thermal unfolding of the enzyme. These changes in T_m and ΔH_{vH}^{U} values originated from changes in the ionization state of the charged protein residues. The acidification of the buffer solution (pH 9.4→5.4) provided an increase in the protein thermal denaturation temperature value, which corresponded to an incremental change of ~10 K, as well as an increase of 200 kJ·mol^{-1} in the value of van't Hoff's enthalpy variation. This increase in the T_m value characterized an improvement in the thermal stability of DdlB in buffering conditions of a pH close to the theoretical isoelectric point of the enzyme (theoretical pI of 5.0). Literature has reported a similar behavior in the T_m and pH ratio for *Trichoderma reesei* cellobiohydrolase Cel7A (theoretical pI of 4.32), which exhibited an improvement in its thermal stability with ΔT_m of ~30 K for a pH range from 9.0 to 3.5 [30]. The theoretical isoelectric points were calculated on the ProtParam webserver [24].

The CD experiments suggest that the DdlB thermal unfolding process was not reversible, since, after the enzyme was subjected to a temperature above its melting temperature, the enzyme did not exhibit a spectral profile similar to its native form (data not shown). This aspect of irreversible denaturation and the increase in β structures at high temperatures (such as 363 K) point to the formation of protein aggregates throughout the process. The increase in the percentage of β-sheet/β-strand may be related to the formation of β intermolecular structures that contribute to the formation and stabilization of aggregates. Such behavior was also observed for the human DNA/RNA-binding KIN protein [31] and human serum albumin [32].

3.4. Dependence of the scanning rate for the thermal denaturation process of DdlB investigated by DSC

Fig. 8a shows the DSC thermograms of the thermal denaturation processes of *Ec*DdlB at a pH of 7.4 and at concentrations of 0.5 and 1.0 mg·mL^{-1} with heating rates of 0.5 and 1.0 K·min^{-1}. All *Ec*DdlB thermograms showed characteristics typical of an endothermic transition composed of a single Gaussian curve. This aspect differed from the complex profile of the thermal denaturation curve determined by the circular dichroism technique, suggesting that the CD data of the enzyme at a pH of 7.4 is a particular and anomalous case, possibly arising from the particular characteristics of the investigated chromophore.
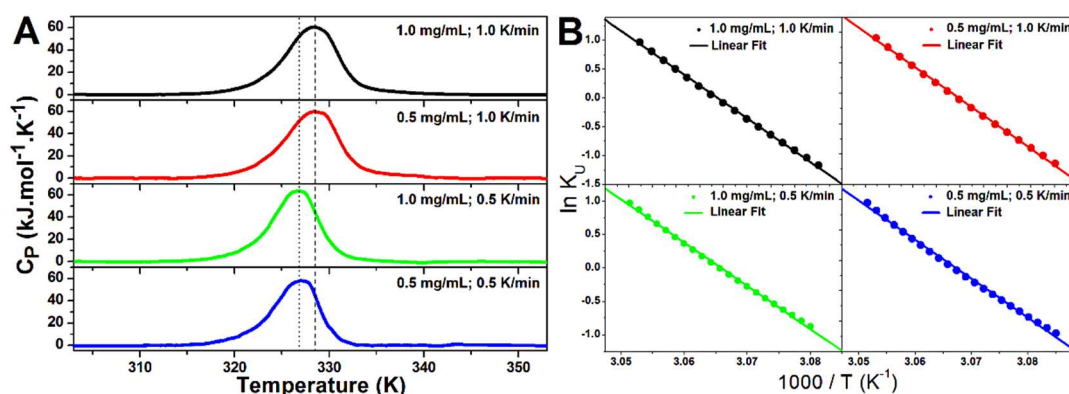
Fig. 8. (**A**) DSC thermograms of *Ec*DdlB at concentrations of 0.5 and 1.0 mg·mL^{-1} for experiments performed with a heating rate of 0.5 and 1.0 K·min^{-1}. The dotted line represents the melting temperature of the thermograms collected at 0.5 K·min^{-1} and the dashed line represents the experiments collected at 1.0 K·min^{-1}. (**B**) Van't Hoff plots of DSC data for thermal denaturation of the enzyme. The filled circles represent the experimental data and the lines denote the adjustment of Equation 6.

Analysis of the thermograms regarding the thermal denaturation temperature (T_m); variation in calorimetric enthalpy (ΔH_{cal}^{U}) and the calculated van't Hoff's enthalpy variations (ΔH_{vH}^{U}), considering a two-state model for the unfolding of DdlB (Fig. 8b), can be seen in Table 2 for two DdlB concentrations and heating rates. The reversibility experiments (cooling scan) showed that the thermal transition of *Ec*DdlB at concentrations of 0.5 and 1.0 mg·mL^{-1} was irreversible.

Table 2
Biophysical parameters obtained by analysis of thermograms in DSC experiments for two
*Ec*DdlB concentrations - [DdlB] - and two heating rates.

[DdlB]/heating rate (mg.mL^{-1}/K.min^{-1})	T_m (ºC)	ΔH_{cal}^{U} (kJ·mol^{-1})	ΔH_{vH}^{U} (kJ·mol^{-1})
1.0/1.0	328.4 ± 0.1 K (55.2)	456 ± 22	471 ± 14
1.0/0.5	326.8 ± 0.1 K (53.7)	418 ± 20	538 ± 16
0.5/1.0	328.4 ± 0.1 K (55.2)	465 ± 23	454 ± 13
0.5/0.5	326.7 ± 0.1 K (53.7)	368 ± 18	534 ± 16

From the thermodynamic parameters (T_m, ΔH_{cal}^{U}, ΔH_{vH}^{U}, and $\Delta H_{cal}^{U} / \Delta H_{vH}^{U}$) determined by the DSC technique, it was possible to observe that the different scanning rates of DSC promoted changes in the DdlB thermal unfolding process. The T_m value showed an average difference of 1.65 K between DSC thermograms collected at 0.5 and 1.0 K·min^{-1}, whereas the ΔH_{cal}^{U} and ΔH_{vH}^{U} revealed an average difference of 68 and 74 kJ·mol^{-1}, respectively. The ratio $\Delta H_{cal}^{U} / \Delta H_{vH}^{U}$ for 0.5 mg·mL^{-1} of enzyme was 0.69 and 1.02, and for 1.0 mg·mL^{-1} was 0.78 and 0.97 in measurements with a heating rate of 0.5 and 1.0 K·min^{-1}, respectively.

It is worth mentioning that the energies ΔH_{cal}^{U} and ΔH_{vH}^{U} are independent and model-dependent thermodynamic parameters, respectively, and therefore the ratio $\Delta H_{cal}^{U} / \Delta H_{vH}^{U}$ denotes the number of moles of the denaturing cooperative unit by the number of moles of the monomer. The expected value of the ratio $\Delta H_{cal}^{U} / \Delta H_{vH}^{U}$ for a transition of two states of a monomer would be equal to 1.0, whereas for a dimer this expected value would be 0.5 [33]. Therefore, it is possible to observe that the ratio $\Delta H_{cal}^{U} / \Delta H_{vH}^{U}$ obtained for the thermal unfolding of DdlB at 0.5 K·min^{-1} was at least 1.5 times greater than the expected value (equal to 0.5) and at least 2 times greater for the process at 1.0 K·min^{-1}. Dependence among $\Delta H_{cal}^{U} / \Delta H_{vH}^{U}$ and the scan rate (0.5 or 1.0 K·min^{-1}) of DSC experiments was characteristic of the kinetic phenomenon of protein aggregation that probably occurs throughout the process of thermal denaturation and intensifies at high temperatures. This result is in agreement with the dependence between T_m and the DSC scan rate, since the formation of aggregates is also dependent on the heating rate developed in the thermal denaturation experiments and, therefore, corroborates the irreversibility characteristic of the process [34].

The biological unit of the crystalized protein DdlB (PDB ID: 4C5C) revealed a homodimeric arrangement with a geometric radius of ~3.8 nm, this result corroborates the DLS measurements that determined a hydrodynamic radius of 4.2 ± 0.1 nm for the protein in solution (Fig. 9), as well as the estimated molecular weight of the protein in solution (Fig. 2b). The smaller radius found in the crystal structure is probably caused by the effect of the reagents used in the crystallization process, such as polyethylene glycol (PEG), in which it acts by removing the solvation water from the surface of the protein to promote crystal nucleation, resulting in compaction of the protein structure [35].
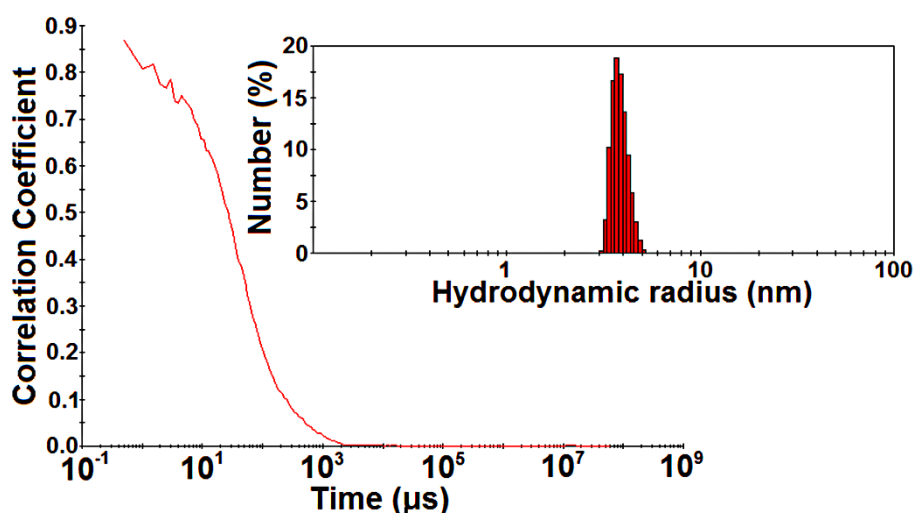
Fig. 9. DLS measurement at 2.0 mg·mL^{-1} of *Ec*DdlB at a pH of 7.4 and at 20 ºC . The insert shows the hydrodynamic radius (nm) distribution profile of the protein in solution. The main plot shows the raw data from the DLS experiment that corresponds to the sigmoidal curve of the correlation coefficient as a function of time (µs).

4. Discussion

Regarding the biophysical parameters obtained from CD analysis of DdlB, the most uncommon behavior was the unusual transition formed by two sigmoidal contributions at a pH of 7.4 (Figure 5b). To interpret this result, we must consider that CD spectra assesses folding of the secondary structure of the protein. Thus, a probable hypothesis to justify this result would be the previous presence of ATP or ADP strongly bound to DdlB during its expression by *E. coli*, where this ligand would not have been totally removed during enzyme purification, gel filtration, buffer exchange, and concentration procedures. Thus, although the experimental conditions in CD analysis were carried out without adding ATP/ADP, a residual amount of this cofactor may still have been previously bonded to DdlB.

We hypothesized that with the rising temperature, close to 320.1 K (47.1 °C), ATP/ADP would start to unbind from the protein and promote a rearrangement in its secondary structure. After the cofactor released, the secondary structure would return to an arrangement similar to that observed at the time when the ATP/ADP began to unbind and, from then on, the CD started to register only the signal variation regarding denaturation of the protein structure. Since the fluorescence analysis does not depend only on secondary structure folding, but mainly on the exposure of the side chains of the chromophoric amino acid residues to the solvent during the denaturation process, this two-step transition observed in CD was not observed in the fluorescence experiment (Fig. 7). This hypothesis is supported by the anomalous behavior only observed at a pH of 7.4 because at this pH, the enzyme EcDdlB would be in its native structure, soaked in a pH value included in the range of cytosolic pH of *Escherichia coli* around 7.2–7.8 [36]. That is, only at a pH of 7.4, among those tested, the DdlB protein would have the correct structural conformation for binding to the ATP/ADP cofactor.

Another curious data obtained in the CD experiments are the percentages of secondary structure found (Table 1). The percentages found to DdlB at pH 5.4 and 9.4 are more resemble the crystallographic model than at pH 7.4, which is closer to the pH 8.0 used to obtain the model. Our group hypothesized two explanations for this data: the first one, is that there is nothing special about the structure at pH 7.4. The bias observed in the CD analysis at this pH does not allow us to correctly identify the percentages of secondary structure. It could be that the structural characteristics in 7.4 are very similar to pH 5.4 and 9.4, but due to the presence of the chromophoric agent linked to the EcDdlB structure, it modifies the CD signal. The second hypothesis is that the 4C5C model is biased due to the compaction process caused by the crystallization process, which is largely due to the high ionic strength and the use of PEG 6000 in the crystallization buffer. Several articles in the literature demonstrated that the use of PEG can cause changes in the native structure of proteins [37–39]. Some works have demonstrated the stabilizing effect of PEG on α-helix structures, which could explain the gain of this secondary structure in detriment of β-turns in the crystallographic model [40,41]. More experiments will be carried out to better evaluate the behavior of EcDdlB at pH 7.4, such as the use of Fourier transform infrared (FTIR) spectroscopy.

The physiological implication of these results presented in this study are that at temperatures of a feverish situation (between 37 to 41 °C), EcDdlB is still active in the

bacterium. Thus, highlighting the need to search for new drugs that can inhibit or reduce its activity.

5. Conclusion

The biophysical analyses carried out in this study have provided for the first time information about the parameters Tm, ΔH^U_{cal}, ΔH^U_{vH}, and characterization of the secondary structure elements in solution for three different pH levels for the enzyme EcDdlB. Additionally, this work well illustrated the relevance of using different techniques in synergy for the analysis of protein structure, only then, it was possible to verify the anomalous behavior of DdlB in CD experiments. The divergences found in the percentages of secondary structure between the protein at pH 7.4 and the crystallographic model highlight the importance of using protein analysis in solution to validate the crystallographic structure that will be used for molecular docking assays. At pH levels of 9.4 and 5.4, a greater structural composition of α-helices regarding β-sheets was found, which was different from that observed at a pH of 7.4 (cytoplasmic pH), where an equal composition was found. An increase in the stability of the protein was observed at lower pH, with greater stability at a pH of 5.4. Such results will be useful for energy minimization of structural models aimed at virtual screening simulations, seeking secondary structure compositions close to those found at pH 7.4, where DdlB is in its native conformation. The results presented here could provide useful information in the search for drugs that inhibit peptidoglycan synthesis.

Conflict of interest

Author declares that no conflict of interest exists.

6. References

[1]   J. Davies, D. Davies, Origins and Evolution of Antibiotic Resistance, Microbiology and Molecular Biology Reviews. 74 (2010) 417–433. https://doi.org/10.1128/MMBR.00016-10.

[2]   D.S. Cayley, H.J. Guttman, M.T. Record, Biophysical characterization of changes in amounts and activity of Escherichia coli cell and compartment water and turgor pressure in response to osmotic stress, Biophysical Journal. 78 (2000) 1748–1764. https://doi.org/10.1016/s0006-3495(00)76726-9.

[3]   K.H. Schleifer, O. Kandler, Peptidoglycan types of bacterial cell walls and their taxonomic implications., Bacteriological Reviews. 36 (1972) 407–477. https://doi.org/10.1128/mmbr.36.4.407-477.1972.

[4]   M. Pazos, K. Peters, Peptidoglycan, in: Subcellular Biochemistry, 2019: pp. 127–168. https://doi.org/10.1007/978-3-030-18768-2_5.

[5]   M.P. Lambert, F.C. Neuhaus, Mechanism of D-cycloserine action: alanine racemase from Escherichia coli W., Journal of Bacteriology. 110 (1972) 978–987. https://doi.org/10.1128/jb.110.3.978-987.1972.

[6]   J.B. Bruning, A.C. Murillo, O. Chacon, R.G. Barletta, J.C. Sacchettini, Structure of the Mycobacterium tuberculosis D-alanine:D-alanine ligase, a target of the antituberculosis drug D-cycloserine, Antimicrobial Agents and Chemotherapy. 55 (2011) 291–301. https://doi.org/10.1128/AAC.00558-10.

[7]   C.T. Walsh, Enzymes in the D-alanine branch of bacterial cell wall peptidoglycan assembly, Journal of Biological Chemistry. 264 (1989) 2393–2396.

[8]   C. Fan, P.C. Moews, C.T. Walsh, J.R. Knox, Vancomycin resistance: Structure of D-alanine:D-alanine ligase at 2.3 Å resolution, Science. 266 (1994) 439–443. https://doi.org/10.1126/science.7939684.

[9]   Y. Shi, C.T. Walsh, Active Site Mapping of Escherichia coli D-Ala-D-Ala Ligase by Structure-Based Mutagenesis, Biochemistry. 34 (1995) 2768–2776. https://doi.org/10.1021/bi00009a005.

[10]   A. Kovač, V. Majce, R. Lenaršič, S. Bombek, J.M. Bostock, I. Chopra, S. Polanc, S. Gobec, Diazenedicarboxamides as inhibitors of d-alanine-d-alanine ligase (Ddl), Bioorganic and Medicinal Chemistry Letters. 17 (2007) 2047–2054. https://doi.org/10.1016/j.bmcl.2007.01.015.

[11]   D. Wu, Y. Kong, C. Han, J. Chen, L. Hu, H. Jiang, X. Shen, d-Alanine:d-alanine ligase as a new target for the flavonoids quercetin and apigenin, International Journal of Antimicrobial Agents. 32 (2008) 421–426. https://doi.org/10.1016/j.ijantimicag.2008.06.010.

[12]   S. Batson, C. De Chiara, V. Majce, A.J. Lloyd, S. Gobec, D. Rea, V. Fülöp, C.W. Thoroughgood, K.J. Simmons, C.G. Dowson, C.W.G. Fishwick, L.P.S. De Carvalho, D.I. Roper, Inhibition of D-Ala:D-Ala ligase through a phosphorylated form of the antibiotic D-cycloserine, Nature Communications. 8 (2017) 1939. https://doi.org/10.1038/s41467-017-02118-7.

[13]   F.C. Neuhaus, J.L. Lynch, The Enzymatic Synthesis of d-Alanyl-d-alanine. III. On the Inhibition of d-Alanyl-d-alanine Synthetase by the Antibiotic d-Cycloserine, Biochemistry. 3 (1964) 471–480. https://doi.org/10.1021/bi00892a001.

[14]   T. Fujihira, S. Kanematsu, A. Umino, N. Yamamoto, T. Nishikawa, Selective increase in the extracellular d-serine contents by d-cycloserine in the rat medial frontal cortex, Neurochemistry International. 51 (2007) 233–236. https://doi.org/10.1016/j.neuint.2007.06.003.

[15]   N.E. Cáceres, N.B. Harris, J.F. Wellehan, Z. Feng, V. Kapur, R.G. Barletta, Overexpression of the D-alanine racemase gene confers resistance to D- cycloserine in Mycobacterium smegmatis, Journal of Bacteriology. 179 (1997) 5046–5055. https://doi.org/10.1128/jb.179.16.5046-5055.1997.

[16]   S.K. Sharma, A. Mohan, Multidrug-resistant tuberculosis, Indian Journal of Medical Research. 120 (2004) 354–376. https://doi.org/10.5124/jkma.2006.49.9.790.

[17]   C. Lange, K. Dheda, D. Chesov, A.M. Mandalakas, Z. Udwadia, C.R. Horsburgh, Management of drug-resistant tuberculosis, The Lancet. 394 (2019) 953–966. https://doi.org/10.1016/S0140-6736(19)31882-3.

[18]   T.T.N. Doan, J.K. Kim, H.P.T. Ngo, H.T. Tran, S.S. Cha, K. Min Chung, K.H. Huynh, Y.J. Ahn, L.W. Kang, Crystal structures of d-alanine-d-alanine ligase from Xanthomonas oryzae pv. oryzae alone and in complex with nucleotides, Archives of Biochemistry and Biophysics. 545 (2014) 92–99. https://doi.org/10.1016/j.abb.2014.01.009.

[19]   C. Cavasotto, A. Orry, R. Abagyan, The Challenge of Considering Receptor Flexibility in Ligand Docking and Virtual Screening, Current Computer Aided-Drug Design. 1 (2005) 423–440. https://doi.org/10.2174/157340905774330291.

[20]   B. Waszkowycz, D.E. Clark, E. Gancia, Outstanding challenges in protein-ligand docking and structure-based virtual screening, Wiley Interdisciplinary Reviews: Computational Molecular Science. 1 (2011) 229–259. https://doi.org/10.1002/wcms.18.

[21]   A. Lavecchia, C. Giovanni, Virtual Screening Strategies in Drug Discovery: A Critical Review, Current Medicinal Chemistry. 20 (2013) 2839–2860. https://doi.org/10.2174/09298673113209990001.

[22]   U. Rester, From virtuality to reality - Virtual screening in lead discovery and lead optimization: A medicinal chemistry perspective, Current Opinion in Drug Discovery and Development. 11 (2008) 559–568.

[23]   S. Batson, D. Rea, V. Fülöp, D.I. Roper, Crystallization and preliminary X-ray analysis of a d-alanyl-d-alanine ligase (EcDdlB) from Escherichia coli, Acta Crystallographica Section F: Structural Biology and Crystallization Communications. 66 (2010) 405–408. https://doi.org/10.1107/S1744309110003970.

[24]   M.R. Wilkins, E. Gasteiger, A. Bairoch, J.C. Sanchez, K.L. Williams, R.D. Appel, D.F. Hochstrasser, Protein identification and analysis tools in the ExPASy server., Methods in Molecular Biology (Clifton, N.J.). 112 (1999) 531–552. https://doi.org/10.1385/1-59259-584-7:531.

[25]   J. Villén, S.P. Gygi, The SCX/IMAC enrichment approach for global phosphorylation analysis by mass spectrometry, Nature Protocols. 3 (2008) 1638. https://doi.org/10.1038/nprot.2008.150.

[26]   Lnb. (2019) Protocols, in solution digestion protocol from Cristea lab, Group. 6 (n.d.)   6–7.   https://lnbio.cnpem.br/wp-content/uploads/2012/11/protocolo_digestao_solucao.pdf (accessed March 1, 2019).

[27]   E. Haid, P. Lehmann, J. Ziegenhorn, Molar absorptivities of β NADH and β NAD at 260 nm, Clinical Chemistry. 21 (1975) 884–887. https://doi.org/10.1093/clinchem/21.7.884.

[28]   N. Sreerama, R.W. Woody, Estimation of protein secondary structure from circular dichroism spectra: Comparison of CONTIN, SELCON, and CDSSTR methods with an expanded reference set, Analytical Biochemistry. 287 (2000) 252–260. https://doi.org/10.1006/abio.2000.4880.

[29]   L. Willard, A. Ranjan, H. Zhang, H. Monzavi, R.F. Boyko, B.D. Sykes, D.S. Wishart, VADAR: A web server for quantitative evaluation of protein structure quality, Nucleic Acids Research. 31 (2003) 3316–3319. https://doi.org/10.1093/nar/gkg565.

[30]   H. Boer, A. Koivula, The relationship between thermal stability and pH optimum studied with wild-type and mutant Trichoderma reesei cellobiohydrolase Cel7A, European Journal of Biochemistry. 270 (2003) 841–848. https://doi.org/10.1046/j.1432-1033.2003.03431.x.

[31]   J.R. Pattaro Júnior, Í.P. Caruso, Q.A. de Lima Neto, F.F. Duarte Junior, F. dos Santos Rando, E.C.M. Gerhardt, M.A. Fernandez, F.A.V. Seixas, Biophysical characterization and molecular phylogeny of human KIN protein, European Biophysics Journal. 48 (2019) 645–657. https://doi.org/10.1007/s00249-019-01390-3.

[32]   R. WETZEL, M. BECKER, J. BEHLKE, H. BILLWITZ, S. BöHM, B. EBERT, H. HAMANN, J. KRUMBIEGEL, G. LASSMANN, Temperature Behaviour of Human Serum Albumin, European Journal of Biochemistry. 104 (1980) 469–478. https://doi.org/10.1111/j.1432-1033.1980.tb04449.x.

[33]   P.L. Privalov, S.A. Potekhin, [2]Scanning microcalorimetry in studying temperature-induced changes in proteins, Methods in Enzymology. 131 (1986) 4–51. https://doi.org/10.1016/0076-6879(86)31033-4.

[34]   A. Cooper, M.A. Nutley, A. Wadood, Differential scanning microcalorimetry in S. E. Harding and B. Z. Chowdhry (Eds.), Protein-Ligand Interactions: hydrodynamics and calorimetry., Oxford University Press, Oxford New York. (2000) 287–318.

[35]   W.J. Ray, C.E. Bracker, Polyethylene glycol: Catalytic effect on the crystallization of phosphoglucomutase at high salt concentration, Journal of Crystal Growth. 76 (1986) 562–576. https://doi.org/10.1016/0022-0248(86)90173-9.

[36]   J.C. Wilks, J.L. Slonczewski, pH of the cytoplasm and periplasm of Escherichia coli: Rapid measurement by green fluorescent protein fluorimetry, Journal of Bacteriology. (2007). https://doi.org/10.1128/JB.00615-07.

[37]   S. Fatima, R.H. Khan, Effect of polyethylene glycols on the function and structure of thiol proteases, Journal of Biochemistry. 142 (2007) 65–72. https://doi.org/10.1093/jb/mvm108.

[38]   V. Kumar, V.K. Sharma, D.S. Kalonia, Effect of polyols on polyethylene glycol (PEG)-induced precipitation of proteins: Impact on solubility, stability and conformation, International Journal of Pharmaceutics. 366 (2009) 38–43. https://doi.org/10.1016/j.ijpharm.2008.08.037.

[39]   S. Rawat, C. Raman Suri, D.K. Sahoo, Molecular mechanism of polyethylene glycol mediated stabilization of protein, Biochemical and Biophysical Research Communications. 392 (2010) 561–566. https://doi.org/10.1016/j.bbrc.2010.01.067.

[40]   A. Koutsioubas, D. Lairez, S. Combet, G.C. Fadda, S. Longeville, G. Zalczer, Crowding effect on helix-coil transition: Beyond entropic stabilization, Journal of Chemical Physics. 136 (2012). https://doi.org/10.1063/1.4723871.

[41]   L.Y. Rivera-Najera, G. Saab-Rincón, M. Battaglia, C. Amero, N.O. Pulido, E. García-Hernández, R.M. Solórzano, J.L. Reyes, A.A. Covarrubias, A group 6 late embryogenesis abundant protein from common bean is a disordered protein with extended helical structure and oligomer-forming properties, Journal of Biological Chemistry. 289 (2014) 31995–32009. https://doi.org/10.1074/jbc.M114.583369.

7. Supplementary data

Biophysical characterization of recombinant *Escherichia coli* D-alanyl,D-alanine ligase B

José Renato Pattaro Júnior[a], Ícaro Putinhon Caruso[b,c], Jéssica Maróstica de Sá[b], Taniara Suelen Mezalira[a], Diego de Souza Lima[a], Eduardo Jorge Pilau[d], David Roper[e], Maria Aparecida Fernandez[f], Flavio Augusto Vicente Seixas[a*]

[a]Departament of Technology, Universidade Estadual de Maringá, Umuarama, PR, Brazil
[b]Department of Physics, Instituto de Biociências, Letras e Ciências Exatas – Universidade Estadual Paulista "Júlio de Mesquita Filho", São José do Rio Preto, SP, Brazil
[c]National Center for Nuclear Magnetic Resonance of Macromolecules, Institute of Medical Biochemistry and National Center for Structure Biology and Bioimaging (CENABIO), Universidade Federal do Rio de Janeiro, Ilha do Fundão, Rio de Janeiro, RJ, Brazil
[d]Departament of Chemistry, Universidade Estadual de Maringá, Maringá, PR, Brasil.
[e]School of Life Sciences, The University of Warwick, Coventry, United Kingdom
[f]Departament of Biotechnology, Genetics and Cell Biology, Universidade Estadual de Maringá, Maringá, PR, Brazil

*Corresponding Author
Dr. Flávio A. V. Seixas
Av. Ângelo Moreira da Fonseca, 1800, Jd Universitário
87506-370, Umuarama, PR, Brazil
+55 44 3621 9337
favseixas@uem.br

Table S1

Mass peptide fingerprint from *Ec*DDlB by LC-MS^E. Red peptides in the sequence matches those founds by LC-MS^E. The yellow highlighted represents an alternative peptide produced by protein digestion that superimpose other peptide sequences.

Protein	Species	Score	Peptides Number	Peptides Sequences	Monoisotopic mass (Mr)
DDLB	ECOLI (K12)	35680	19	K.IAVLLGGTSAER.E(+2), R.EVSLNSGAAVLAGLR.E(+2), R.EGGIDAYPVDPK.E(+2), K.EVDVTQLK.S(+2), K.VFIALHGR.G(+2), R.AEFEKGLSDK.Q(+2), R.EGSSVGMSK.V(+2), K.VVAENALQDALR.L(+2), R.LAFQHDEEVLIEK.W(+2), K.WLSGPEFTVAILGEEILPSIR.I(+2) R.IQPSGTFYDYEAK.Y(+2), K.YLSDETQYFCPAGLEASQEANLQALVLK.A(+2, K.AWTTLGCK.G(+2), R.IDVMLDSDGQFYLLEANTSPGMTSHSLVPMAAR.Q(+2), R.QAGMSFSQLVVR.I(+2) R.GGEDGTLQGMLELMGLPYTGSGVMASALSMDK.L°+ Oxidation (M)(+2), R.SKLLWQGAGLPVAPWVALTR.A(+2), K.LLWQGAGLPVAPWVALTR.A(+2), K.GLSDKQLAEISALGLPVIVKPSR.E(+2), K.QLAEISALGLPVIVKPSR.E(+2)	32,933

>sp|P07862|DDLB_ECOLI D-alanine--D-alanine ligase B OS=Escherichia coli (strain K12) OX=83333 GN=ddlB PE=1 SV=3
MTDK**IAVLLGGTSAER**EVSLNSGAAVLAGLR**EGGIDAYPVDPK**EVDVTQLKSMGFQK**VFI
ALHGR**GGEDGTLQGMLELMGLPYTGSGVMASALSMDK**LR**SKLLWQGAGLPVAPWVALTR**A
EFEK**GLSDK**QLAEISALGLPVIVKPSR**EGSSVGMSK**VVAENALQDALR**LAFQHDEEVLIE
K**WLSGPEFTVAILGEEILPSIR**IQPSGTFYDYEAK**YLSDETQYFCPAGLEASQEANLQAL
VLK**AWTTLGCK**GWGR**IDVMLDSDGQFYLLEANTSPGMTSHSLVPMAAR**QAGMSFSQLVVR**
ILELAD

Atividade antiviral do extrato de *Poincianella pluviosa* contra SARS-CoV-2

José Renato Pattaro Júnior[1]; Ingrid Garcia Araújo[1]; Carolina Borsoi Moraes[3]; Gisele Strieder Philippsen[2]; Lucio Holanda Gondim de Freitas Junior[3]; João Carlos Pallazo de Mello[4]; Rosane Marina Peralta[5]; Maria Aparecida Fernandez[6]; Róbson Ricardo Teixeira[7]; Flavio Augusto Vicente Seixas[1]*

[1]Departamento de Tecnologia, Universidade Estadual de Maringá, Umuarama, PR, Brasil
[2]Universidade Federal do Paraná, Jandaia do Sul, PR, Brasil.
[3]Instituto de Ciências Biomédicas, Universidade de São Paulo, São Paulo, Brasil
[4]Departamento de Farmácia, Universidade Estadual de Maringá, Maringá, PR, Brasil
[5]Departamento de Bioquímica, Universidade Estadual de Maringá, Maringá, PR, Brasil
[6]Departamento de Biotecnologia, Genética e Biologia Celular, Universidade Estadual de Maringá, Maringá, PR, Brasil
[7]Departamento de Química, Universidade Federal de Viçosa, Viçosa, MG, Brasil

*Autor de Correspondência
Dr. Flavio A. V. Seixas
Av. Ângelo Moreira da Fonseca, 1800, Jd Universitário
87506-370, Umuarama, PR, Brazil
+55 44 3621 9337
favseixas@uem.br

Lista de Abreviações

β-CoVs - β-coronavírus

DAPI - *4',6-diamidino-2-fenilindole*

DMSO - Dimetilsulfóxido

ESI-MS/MS - Espectrometria de Massas com Ionização por Eletropuverização

FAE ou EtOAc – Fração Acetato de Etila

HTS - *High-throughput screening*

HMW - *High Molecular Weight*

IPTG - Isopropil β-D-1-tiogalactopiranosídeo

IR - Taxa de Infecção

LMW – *Low Molecular Weight*

MERS CoV - Coronavírus da Síndrome Respiratória do Oriente Médio

M^{pro} – Protease Principal

NSP – Proteínas Não Estruturais

PDB ID – *Protein data bank Identity*

PFA - Paraformaldeído

PGG - Pentagalloilglicose

RBD - Domínio de Ligação ao Receptor

RMN - Ressonância Magnética Nuclear

SARS - Síndrome Respiratória Aguda Grave

X77 - N-(4-tert-butylphenyl)-N-[(1R)-2-(cyclohexylamino)-2-oxo-1-(pyridin-3-yl)ethyl]-1H-imidazole-4-carboxamide

ABSTRACT

Embora existam vacinas eficientes, não há tratamento antiviral específico para casos graves de Covid-19 que requerem internação em Unidades de Terapia Intensiva (UTI). Devido à carência de fármacos eficientes no tratamento de Covid-19 e à iminência do surgimento de uma cepa viral que seja resistente parcial ou integralmente às vacinas atuais, a protease principal do SARS-CoV-2 (M^{pro}) torna-se um alvo atrativo para novas moléculas antivirais, por apresentar papel chave no ciclo viral e não possuir homologia com proteínas humanas. Assim, este estudo teve o objetivo de prospectar novos compostos inibidores de M^{pro} de SARS-CoV-2 em extratos de *Poincianella pluviosa* e compostos sintéticos, a partir de varredura virtual, e avaliar seu potencial inibitório empregando ensaios proteolíticos em M^{pro} recombinante e ensaios com células Vero E6 infectadas. Nos ensaios de *docking* molecular foram identificados quatro compostos com potencial atividade inibitória de M^{pro}, presentes nos extratos de *P. pluviosa*. O composto isolado Pentagalloylglucose (PGG) apresentou os melhores resultados nos experimentos de cinética proteolítica, com uma supressão da atividade da M^{pro} recombinante em ~60%. No entanto, nos experimentos com células infectadas todas as frações do extrato de *P. pluviosa* (FAE, F4 e F2) performaram melhor que PGG, alcançando ~100% de atividade. A proeminente atividade dos extratos em células infectadas pode ter sido ocasionada pelo efeito sinérgico dos diversos taninos hidrolisáveis presentes, com ação simultânea em M^{pro} e outros alvos de SARS-CoV-2 e do hospedeiro.

Palavras-chave: SARS-CoV-2; M^{pro}; Covid-19; taninos antivirais; *Poincianella pluviosa*

1.Introdução

O vírus SARS-CoV-2 pertencente à família altamente diversa *Coronavidae*, mais especificamente, está incluso no gênero β-coronavírus (β-CoVs), no qual muitas espécies são patógenos humanos e causam doenças respiratórias graves, incluindo o SARS-CoV e o Coronavírus da Síndrome Respiratória do Oriente Médio (MERS-CoV) [1]. O genoma de SARS-CoV-2 é composto por RNA de fita simples de senso positivo (+ssRNA) com cerca de 30,000 nucleotídeos. Após a entrada na célula hospedeira, este RNA é transcrito a partir de duas ORFs sobrepostas, ORF1a e ORF1b, dando origem às poliproteínas pp1a e pp1ab, respectivamente, que são requeridas para a replicação e transcrição viral [2–4]. Os polipeptídeos funcionais são liberados das poliproteínas pp1a e pp1ab por extenso processamento proteolítico, sendo clivados em 16 proteínas não estruturais (NSP), predominantemente por uma cisteíno protease de 33.8 kDa denominada M^pro (também conhecida como 3 cysteine-like protease – 3CL^pro).

M^pro (EC 3.4.22.69) hidrolisa pelo menos 11 sítios conservados na poliproteína pp1ab, começando pelo seu sítio de clivagem autolítica [5]. Seu sítio de clivagem demonstra certa promiscuidade, reconhecendo motivos com sequência contendo LXGG|(A/K)X, onde X é qualquer aminoácido e | é o ponto em que ocorre a hidrólise da ligação peptídica [6,7]. Estudos mostraram que a M^pro possui fundamental importância para o ciclo viral, pois inibidores específicos bloquearam o ciclo de vida viral sem biotoxicidade óbvia, devido ao fato da M^pro não possuir homólogos em humanos [8–10].

A investigação da estrutura da M^pro de SARS-CoV-2, utilizando cristalografia de raios X, identificou que a estrutura proteica é altamente semelhante à outras proteínas M^pro de outros coronavírus resolvidas anteriormente, sugerindo a importância fundamental dessa proteína para a família *Coronaviridae* [11–16]. M^pro possui como unidade biológica um homodímero, onde cada monômero é subdividido em três domínios: o Domínio I (resíduos 8-101) e o Domínio II (resíduos 102-184) formam uma arquitetura quimotripsina-like com uma cisteína catalítica e um *loop* longo (resíduos 185-200) os liga ao Domínio III (resíduos 201-303). A região de interação entre os dois monômeros é majoritariamente composta pelo Domínio II de um monômero e os resíduos do N-terminal do outro, o que favorece a formação do bolso de ligação ao substrato [17,18].

Por apresentar papel chave no ciclo viral e não possuir homologia com proteínas humanas, a M^{pro} de SARS-CoV-2 torna-se um alvo atrativo para novas moléculas antivirais. Diversos grupos de pesquisa estão reportando a identificação de compostos promissores com atividade inibitória de M^{pro} a partir de ensaios com combinação de varredura virtual baseada em estrutura e triagem de alto rendimento (HTS - *High-throughput screening*) [11,19–21]. No entanto, a taxa de sucesso das drogas que iniciam os estudos e que, de fato, se tornam medicamentos ao término de todas as etapas dos testes clínicos é de apenas 12%, aproximadamente [22]. Adicionalmente, alguns tratamentos já foram identificados; entretanto, possuem baixa eficácia clínica ou requerem utilização dentro de uma janela de tratamento estreita [23,24], tornando a pesquisa continuada de novas terapêuticas essencial.

Diversos estudos com produtos naturais vêm dando luz a metabólitos secundários de plantas com atividade antiviral [25,26]. Um destes metabólitos são os taninos, compostos encontrados na maioria das plantas superiores e produzidos em quase todas as partes da planta, por causa de seu papel fundamental na defesa contra insetos, fungos, vírus ou bactérias [27]. Diversos trabalhos na literatura já demonstraram a atividade antiviral de taninos [28–30], inclusive contra o vírus SARS-CoV-2 [31]. Os taninos também podem auxiliar na melhora do quadro de pacientes com Covid-19 (também considerado um distúrbio inflamatório), devido as suas atividades antioxidantes e antiinflamatórias, assim, podem diminuir a morbidade e mortalidade da doença [32]. Por mais que alguns compostos antivirais pareçam ser promissores, são poucos os extratos de espécies vegetais da flora brasileira que foram caracterizados e, portanto, constituem um campo de pesquisa pouco explorado no combate a infecções por microrganismos.

Devido à carência de fármacos eficientes no tratamento de casos graves de Covid-19 e à iminência do surgimento de uma cepa viral que seja resistente parcial ou integralmente às vacinas atuais, este estudo teve o objetivo de prospectar novos inibidores da enzima M^{pro} de SARS-CoV-2. A estratégia é utilizar a metodologia de varredura virtual de extratos de *Poincianella pluviosa* (também conhecida como Sibipiruna) e compostos sintéticos, bem como avaliar o potencial inibitório empregando ensaios proteolíticos em M^{pro} expressa heterologamente. Os melhores inibidores da M^{pro} foram avaliados em estudos de atividade antiviral em culturas de células Vero E6 e sua potencial toxicidade *in vitro*. Os compostos apresentados aqui poderão aumentar o acervo de drogas

com potencial atividade antiviral contra este vírus que já resultou em milhões de mortes e vem causando danos econômicos vertiginosos em todo o mundo.

2. Material e Métodos

2.1. Simulações de varredura virtual

A cadeia A da estrutura cristalográfica da protease principal (M^{pro}) de SARS-CoV-2 ligada ao inibidor não covalente *N-(4-tert-butylphenyl)-N-[(1R)-2-(cyclohexylamino)-2-oxo-1-(pyridin-3-yl)ethyl]-1H-imidazole-4-carboxamide* (chamado de X77) - PDB ID: 6W63 [33] - foi utilizada nas simulações de varredura virtual. Para isso, todas as águas e sais foram removidos da estrutura e os programas de varredura com os respectivos protocolos foram definidos por meio de *redocking* do ligante X77 (Pubchem CID 145998279). O programa AutoDock Vina [34] utilizou o algoritmo padrão de busca e ranqueamento com uma caixa de dimensões 15, 20 e 20 nos eixos *x*, *y* e *z*, respectivamente, centrada no ligante X77. Os ligantes foram minimizados usando o campo de força uff [35] antes de serem convertidos para o formato *.pdbqt. O programa Molegro v-6.1 [36] utilizou os algoritmos *Moldock SE* e *Moldock Score* para busca e ranqueamento, respectivamente, onde os ligantes foram ranqueados pelo menor índice H-bond. O raio de busca foi de 9 Å centrado no ligante X77. Os programas foram considerados validados quando o rmsd encontrado na sobreposição do ligante X77 foi menor que 1,5 Å em todas as repetições.

A biblioteca contendo 13 taninos identificados no extrato de *P. pluviosa* [37] e o ligante X77 foram utilizados nas simulações. As estruturas 2D ou 3D dos compostos foram obtidas nas bases de dados Zinc15 ou PubChem [38,39], adicionadas de hidrogênios e convertidas para o formato 3D com o programa OpenBabel [40]. A varredura virtual foi realizada em quadruplicata, com os programas validados, e os escores médios dos compostos avaliados foram ponderados por meio da Equação 1.

$$\text{Escore relativo médio} = \frac{1}{2}\left(\frac{Molegro}{Molegro_{\max}} + \frac{Vina}{Vina_{\max}} \right) \qquad (1)$$

Os termos *Molegro~max~* e *Vina~max~* correspondem à pontuação do composto ao qual o escore numérico máximo foi atribuído por cada programa. O escore médio relativo obtido com o ligante X77 foi utilizado como nota de corte.

2.2. Expressão e purificação da proteína recombinante M^pro^ de SARS-CoV-2

O plasmídeo pET22b-M^pro^ contendo a sequência codificante de M^pro^ (clonado usando as enzimas de restrição NdeI e XhoI) foi adquirido da empresa FastBio (BRA). O plasmídeo foi desenhado para gerar uma proteína quimérica com 6 resíduos de histidina na extremidade C-terminal. As cepas de *Escherichia coli* BL21 (DE3), transformadas com o plasmídeo pET22b+M^pro^, foram cultivadas aerobicamente em meio LB líquido contendo 50 μg.mL^{-1} de ampicilina a 37 ºC. Quando a cultura atingiu OD_{600} de 0,6, foi induzida à expressão de M^pro^ utilizando-se 0,5 mM de IPTG (Isopropil β-D-1-tiogalactopiranosídeo); a cultura foi mantida em 20 ºC por 14 horas. Depois da expressão, a cultura foi centrifugada em 10.000 $\times$ g por 10 min à 4 ºC e o pellet armazenado em freezer -20 ºC.

O pellet foi ressuspenso em tampão de lise (NaH_2PO_4 50 mM, NaCl 300 mM, imidazol 10 mM, 10% glicerol, 0,2% Triton X-100 e pH 8,0) e sonicado por 4 min com pulsos de 20 s ON e 20 s OFF no gelo com amplitude de 60% em sonicador Fisher Scientific. O extrato sonicado foi centrifugado em 15.000 $\times$ g por 10 min à 4 ºC e o sobrenadante foi filtrado em filtro de seringa Millex$^{\circledR}$ de 0,22 μm (Merck-Millipore, GER). Posteriormente, o sobrenadante foi aplicado em HisTrap (Cytiva, USA) de 1 mL usando AKTA Purifier (Cytiva, USA), para a injeção e monitoramento da amostra, em tampão de *binding* (NaH_2PO_4 50 mM, NaCl 300 mM, imidazol 10 mM e pH 8,0). Para a eluição da proteína foi utilizado um gradiente de 10–300 mM imidazol. A análise de purificação foi realizada usando SDS-Page 12% [41].

A verificação da unidade biológica homodimérica de M^pro^ foi realizada a partir da massa da proteína eluída em cromatografia de gel filtração, utilizando coluna Superdex^{TM} Increase 200 10/300 GL (Cytiva, USA). A curva de calibração foi construída usando o kit de calibração de filtração em gel LMW e HMW (Cytiva, USA), seguindo as recomendações do fabricante. A análise foi realizada em modo isocrático utilizando o tampão fosfato 50 mM + NaCl 100 mM (pH 7,2) à temperatura ambiente e fluxo de 0,5 mL/min e o acompanhamento da corrida foi realizado a partir das absorbâncias em 214 e

280 nm. Os volumes de eluição para cada proteína foram medidos e convertidos em K_{av} (Equação 2) e plotados em função do logaritmo dos respectivos pesos moleculares (*log*MW),

$$K_{av} = \frac{V_e - V_o}{V_c - V_o} \tag{2}$$

sendo V_e = volume de eluição, V_o = volume vazio da coluna e V_c = volume geométrico da coluna. As análises foram realizadas em duplicata.

As amostras foram concentradas e tiveram seus tampões trocados em filtros de centrífuga Amicon® com *Cut Off* de 10 kDa (Merck-Millipore, GER) e quantificadas a 280 nm para os ensaios de proteólise, usando um coeficiente de extinção molar de 0,94 L.g⁻¹.cm⁻¹ para conversão de Abs em mg.mL⁻¹ estimado pelo servidor web ProtParam [42].

2.3. Ensaio proteolítico com substrato fluorogênico

O substrato fluorogênico LGSAVLQ-Rh110-dP (Boston Biochem, USA) foi usado como substrato nos ensaios proteolítica *in vitro* com a enzima recombinante Mpro de SARS-CoV-2. A Mpro cliva o C-terminal do aminoácido glutamina (LGSAVLQ| - Rh110-dP), convertendo o substrato de bisamida não fluorescente em monoamida fluorescente e, em seguida, em rodamina 110, com um aumento adicional na fluorescência [43,44]. A rodamina 110 foi monitorada com excitação e emissão nos comprimentos de onda de 485 nm e 535 nm, respectivamente. Foram realizados testes em duplicata sem a presença de inibidores, onde o substrato foi testado na faixa de concentração de 2 a 50 µM, com 1 µM de Mpro em tampão de ensaio (50 mM Tris-HCl, pH 7.5, 1 mM EDTA) com volume final de reação de 300 µL em placa preta de 96 poços (Greiner Bio-One, AUT), sendo conduzido no equipamento FlexStation 3 (Molecular Devices, USA). As velocidades foram ajustadas à equação de Hill adaptada a equação de Michaelis-Menten (Equação 3).

$$V = \frac{Vmax.[S]^n}{Km^n + [S]^n} \tag{3}$$

onde V é a velocidade na concentração de substrato S, $V_{máx}$ é a velocidade máxima, K_M é a constante de Michaelis e n é o coeficiente de Hill.

Os ensaios na presença dos inibidores foram de ponto único, sendo usado 10 μM de substrato fluorogênico, 1 μM de M^{pro} em tampão de ensaio com 5 μL de inibidor a 2.63 mg.mL^{-1} (concentração final de 43.8 μg.mL^{-1}), com volume final de 300 μL. Os extratos de *P. pluviosa* [37] e os compostos sintéticos (Bm6, Bm7, Bm8 e PGG) foram diluídos em DMSO (Dimetilsulfóxido). Os ligantes Bm6, Bm7 e Bm8 foram sintetizados e gentilmente cedidos pelo prof. Róbson Ricardo Teixeira da Universidade Federal de Viçosa (UFV) [45]. O diluente dos inibidores, DMSO, também foi testado para verificar se poderia influenciar a velocidade da reação enzimática. Todos os testes foram incubados por 10 min para que houvesse equilíbrio térmico com a temperatura do ensaio de 37 ℃. O início da reação foi realizado com a introdução da enzima M^{pro}. Todas as corridas foram subtraídas as suas respectivas linhas de base, sendo esta obtida com todos os componentes de cada teste, exceto a M^{pro} de SARS-CoV-2. Todos os experimentos foram realizados utilizando 5 min de tempo de reação, com leitura da fluorescência a cada 10 s.

2.4. Ensaios em células Vero E6 em cultura

Os ensaios dos compostos com células Vero E6 em cultura foram realizados em laboratório NB3 do Instituto de Ciências Biomédicas – ICB - da Universidade de São Paulo (USP). Os compostos foram dissolvidos nas concentrações indicadas e diluídos em série em DMSO. Imediatamente antes do plaqueamento, os compostos foram diluídos $33{,}33 \times$ em PBS, e 10 μL dessas soluções foram transferidos para placas de ensaio.

As células Vero E6 foram semeadas em placas de 384 poços em DMEM High e incubadas durante 24 h. Após a incubação (37 ℃, 5% CO_2), os compostos foram adicionados à placa para atingir uma concentração final de 100 μg/mL. Após a inoculação viral, as placas foram mantidas por 36 h de incubação (37 ℃, 5% CO_2), sendo, posteriormente, fixadas com 4% de PFA (paraformaldeído) e submetidas à imunofluorescência indireta como segue o protocolo adiante. Após lavagem duas vezes com PBS pH 7,4, as placas foram bloqueadas com albumina de soro bovino a 5% (BSA) (Sigma-Aldrich, USA) em PBS (BSA-PBS) por 30 min em temperatura ambiente e lavadas duas vezes com PBS. Como um anticorpo primário, o soro de um paciente brasileiro convalescente de Covid-19 diluído 1:500 em PBS ou um anticorpo policlonal de coelho anti-SARS-CoV-2 proteína nucleocapsídica (GeneTex, USA) a 2 μg/mL em PBS foram usados para detectar a infecção de SARS-CoV-2 em células Vero. Os anticorpos primários foram incubados por 30 min e as placas foram lavadas duas vezes

com PBS. Como anticorpos secundários, IgG anti-humano de cabra marcado com FITC (Chemicon) ou IgG anti-coelho de cabra marcado com Alexa 488 (Thermo Scientific, USA) foi usado diluído a 4 µg/mL em PBS e incubado por 30 min com 5 µg/mL dihidrocloreto de 4',6-diamidino-2-fenilindole (DAPI, Sigma-Aldrich, USA) em PBS para corar núcleos. As placas foram lavadas duas vezes com PBS e fotografadas no Operetta High Content Imaging System (Perkin Elmer, USA) usando uma objetiva de ampliação de 20 ×. Quatro imagens foram adquiridas por poço.

As imagens adquiridas foram analisadas no software Harmony (Perkin Elmer, USA), versão 3.5.2. A análise das imagens consistiu na identificação e contagem de células Vero E6 com base na segmentação nuclear e infecção viral com base na coloração citoplasmática detectada pelo ensaio de imunofluorescência. A taxa de infecção (IR) foi calculada como a razão entre o número de células infectadas e o número total de células contadas em cada poço. A taxa de sobrevivência celular foi calculada como o número de células contadas em cada poço dividido pelo número médio de células nos poços de controle positivo (células infectadas tratadas com DMSO), multiplicado por 100. A atividade antiviral foi determinada pela normalização do IR ao controle negativo (células infectadas e não infectadas tratadas com DMSO), conforme a Equação 4.

$$\% = 100 \times \left(1 - \left(\frac{IR_{test} - IR_{pos}}{IR_{neg} - IR_{pos}}\right)\right) \qquad (4)$$

Sendo: IR_{test} = Taxa de infecção em um dado poço com composto teste; IR_{pos} = Taxa de infecção média do controle positivo (células não infectadas tratadas com veículo); e IR_{neg} = Taxa de infecção média do controle negativo (células infectadas tratada com veículo).

3. Resultados

3.1. Seleção de compostos por docking molecular

A estrutura da M^{pro} ligada ao inibidor X77 (PDB ID: 6W63) foi escolhida, dentre diversas outras, devido ao ligante X77 não estar ligado de forma covalente, o que é um requisito importante na escolha de inibidores por varredura virtual, uma vez que o método

de *docking* simula uma ligação não covalente (inibição competitiva) no sítio ativo da enzima. Esta limitação é devido ao fato de que programas de *docking* utilizados não conseguem fazer varredura virtual em larga escala considerando inibidores que poderiam se ligar de forma covalente.

Os escores médios obtidos com quatro simulações de *docking* para cada um dos ligantes da biblioteca testada, com ambos os programas utilizados, mais o escore médio relativo obtido com a Equação 1 são mostrados na Tabela 1. Em negrito é mostrado o ligante X77.

Tabela 1. Escores médios obtidos com quatro simulações de *docking* da biblioteca de taninos do extrato de *P. pluviosa*.

| Compound Id	Vina escore médio	Molegro escore médio	Escore médio relativo
CID65238	-9,6 ± 0,1	-24,07 ± 1,74	0,99
CID151590	-9,5 ± 0,1	-21,46 ±2,27	0,93
CID73178	-9,3 ± 0,1	-21,00 ±4,18	0,91
CID452707	-9,4 ± 0,1	-21,69 ±5,99	0,93
Zinc4098612	-9,2 ± 0,1	-15,73 ±2,01	0,80
CID3001497	-8,7 ± 0,4	-16,13 ±3,39	0,78
CID73179	-8,7 ± 0,3	-18,81 ±1,55	0,84
CID10056140	-8,4 ± 0,1	-20,56 ±3,56	0,86
CID145998279	**-8,4 ± 0,1**	**-5,14 ±1,52**	**0,87**
CID16131237	-8,2 ± 0,2	-21,39 ±3,03	0,43
CID5281855	-7,3 ± 0,0	-10,25 ±0,11	0,59
Zinc21789	-5,3 ± 0,1	-13,90 ±2,00	0,56
Zinc1504	-5,2 ± 0,0	-15,69 ±0,05	0,59
Zinc330141	-4,8 ± 0,1	-13,37 ±1,60	0,52

Uma representação gráfica dos escores médios relativos ordenados é mostrada na Figura 1. Esta representação ilustra melhor os compostos mais bem ranqueados que o ligante de referência X77.
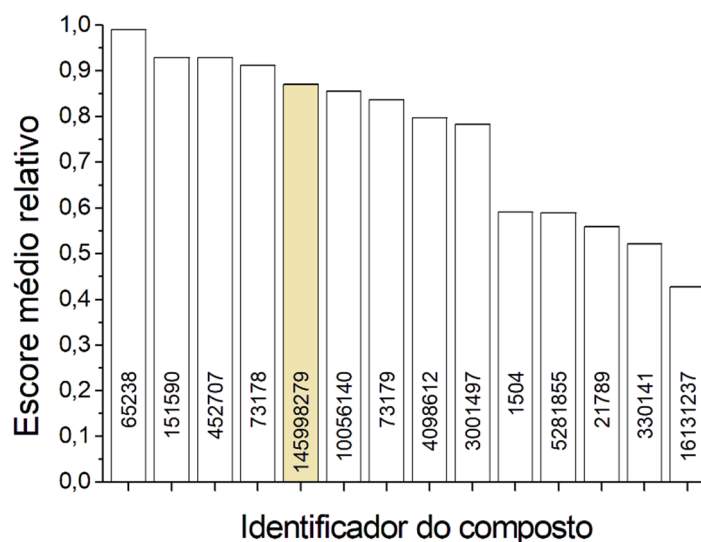
Figura 1. Representação gráfica dos escores médios relativos dos taninos presentes no extrato de *Poincianella pluviosa* em relação ao ligante de referência X77 (CID145998279) marcado em bege.

A Figura 1 e a Tabela 1 mostram que quatro ligantes ficaram mais bem ranqueados do que o ligante de referência X77. O ligante CID 65238 ou Pentagalloylglucose (PGG) foi o melhor avaliado tendo, em teoria, maior probabilidade de se ligar à M^{pro} de SARS-CoV-2 em relação aos demais ligantes. Porém, devido ao seu grande número de ligações rotacionáveis (Figura 2), não foi possível encontrar uma pose constante para sua interação com o sítio ativo da proteína alvo (Figura 3A). Isso pode significar que sua interação com a proteína é inespecífica e que, na prática, poderia apresentar um fenômeno de inibição mista, haja visto que poses diferentes poderiam interagir com a proteína de forma diferente, simulando a interação de ligantes diferentes.
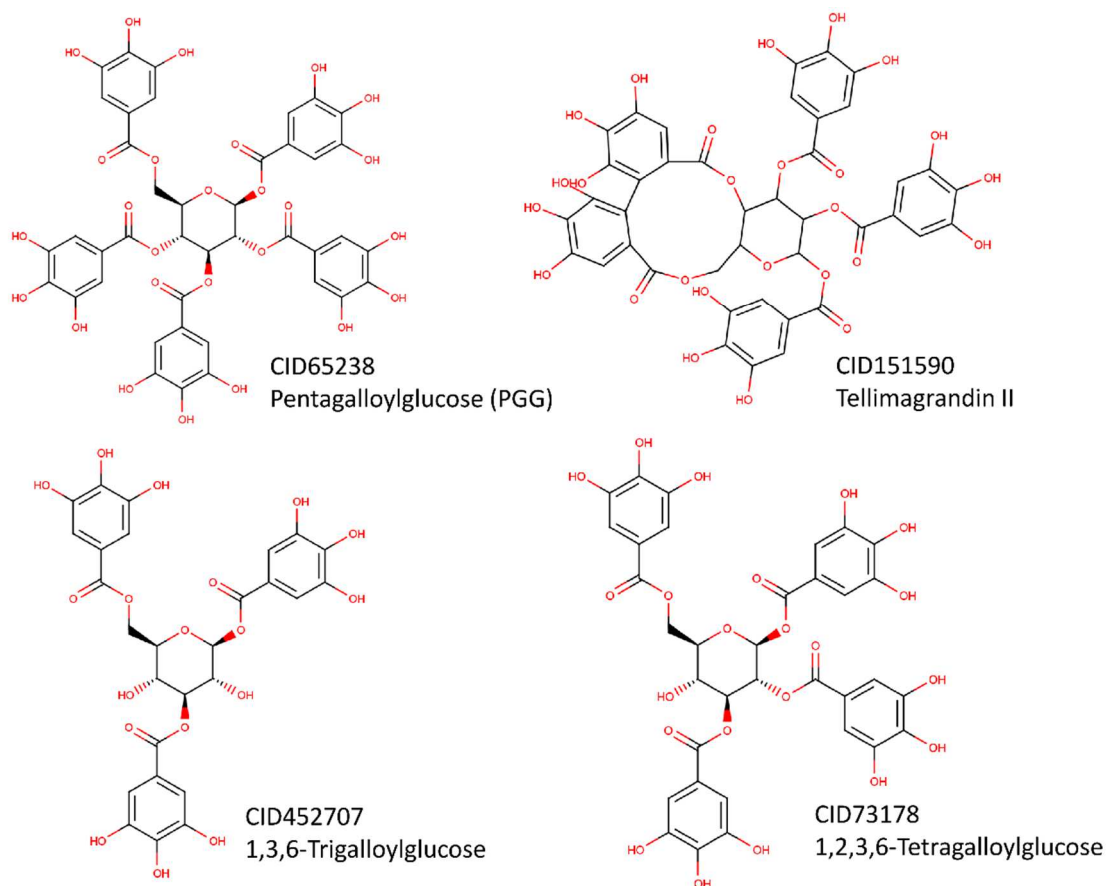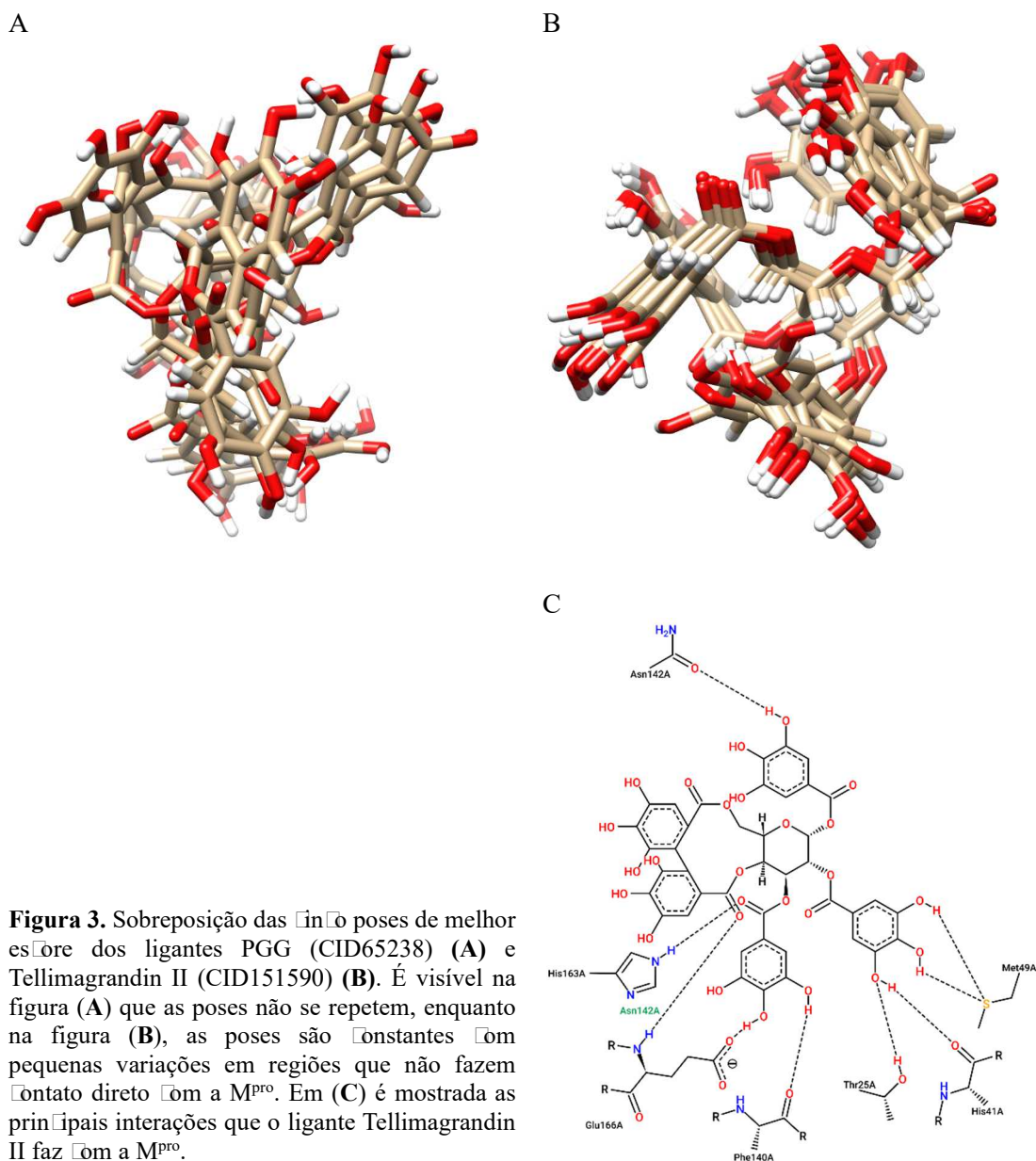
Figura 2. Estrutura dos compostos com melhores escores relativos no *docking* que teve a M^{pro} de SARS-CoV-2 como alvo.

Já o composto CID151590 (Tellimagrandin II), foi o que apresentou o segundo melhor escore relativo e também foi o ligante que apresentou o maior número de poses que se repetiram nas simulações (Figura 3B). Isso pode significar que, apesar de ser um ligante com menor escore relativo que o PGG, há alta probabilidade dele se ligar a M^{pro}, de maneira específica (Figura 3C), devido ao *cluster* de conformações encontradas. Na Figura 3C pode ser verificado que os resíduos do sítio ativo de M^{pro} Thr25, His41, Phe140, Asn142, His163 e Glu166 são responsáveis pela formação de ligações de hidrogênio e Met49 por interação dipolo-dipolo com Tellimagrandin II, sendo o resíduo His41 em conjunto com Cys145 responsáveis pela atividade catalítica (díade catalítica) [46].

Os ligantes CID452707 (1,3,6-Trigalloylglucose) e CID73188 (1,2,3,6-Tetragalloylglucose), apesar dos bons escores relativos, apresentaram um menor número de poses que se repetiram na interação com a enzima, o que também pode significar

interação pouco específica com o sítio ativo da M^{pro}. Os quatro compostos polifenólicos encontrados são depsídeos, polifenóis compostos por duas ou mais unidades aromáticas monocíclicas ligadas por uma ligação éster. Já foi verificado atividade antiviral para essa classe de compostos na literatura para o HIV e o vírus da Hepatite C [47,48].

A

B

C

Figura 3. Sobreposição das cin o poses de melhor es ore dos ligantes PGG (CID65238) **(A)** e Tellimagrandin II (CID151590) **(B)**. É visível na figura (**A**) que as poses não se repetem, enquanto na figura (**B**), as poses são onstantes om pequenas variações em regiões que não fazem ontato direto om a M^{pro}. Em (**C**) é mostrada as prin ipais interações que o ligante Tellimagrandin II faz om a M^{pro}.

Em função destes resultados, a fração acetato de etila (FAE ou fração EtOAc) do extrato de *Poincianella pluviosa*, bem como as subfrações denominadas de F2 e F4 [37] foram utilizadas em ensaios de inibição da M^{pro} recombinante. O composto isolado

Pentagalloylglucose foi sintetizado conforme descrição na literatura [49,50], para ser testado em sua forma pura como inibidor de M^pro.

3.2. Produção e identificação da unidade biológica de M^pro de SARS-CoV-2

Foi verificado um bom rendimento na produção de M^pro, tendo como resultado ~2 mL da proteína pura na concentração de 0,6 – 0,8 mg/mL a cada 100 mL de cultura. A massa da proteína observada em SDS-PAGE 12% está condizente com a massa teórica de 34.992,96 Da (Figura 4), predita pela plataforma ProtParam. A pureza foi considerada satisfatória apenas utilizando a cromatografia de afinidade, já que não foi verificada nenhuma outra banda contaminante em conjunto com M^pro.
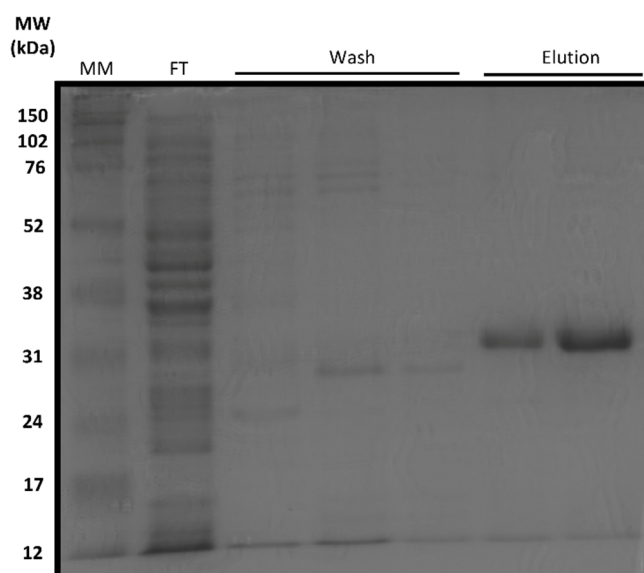
Figura 4. Produção da proteína recombinante M^pro em *E. coli*. A protease purificada foi corrida em SDS-PAGE 12% para confirmar a massa e a pureza. MM - Marcador Molecular (Full Range Rainbow, Cytiva, USA). Wash - tampão de eluição 0–35%, Elution - tampão de eluição 35–100%.

Após a purificação, a proteína foi concentrada a 2 mg.mL^{-1} para o ensaio em cromatografia analítica de gel filtração em coluna Superdex^TM Increase 200 10/300 GL, em modo isocrático. A Figura 5 mostra os volumes de eluição dos padrões e de M^pro que foram convertidos para K_{av} e representados graficamente em relação ao logarítimo de seus massas moleculares. A massa molecular de M^pro foi calculada por ajuste linear, e a massa encontrada para a M^pro recombinante de SARS-CoV-2 foi de 67,182 Da. A razão das massas [homodímero]/[massa teórica monômero] foi de 1.92, sugerindo um homodímero como unidade biológica, o que está de acordo com a literatura.
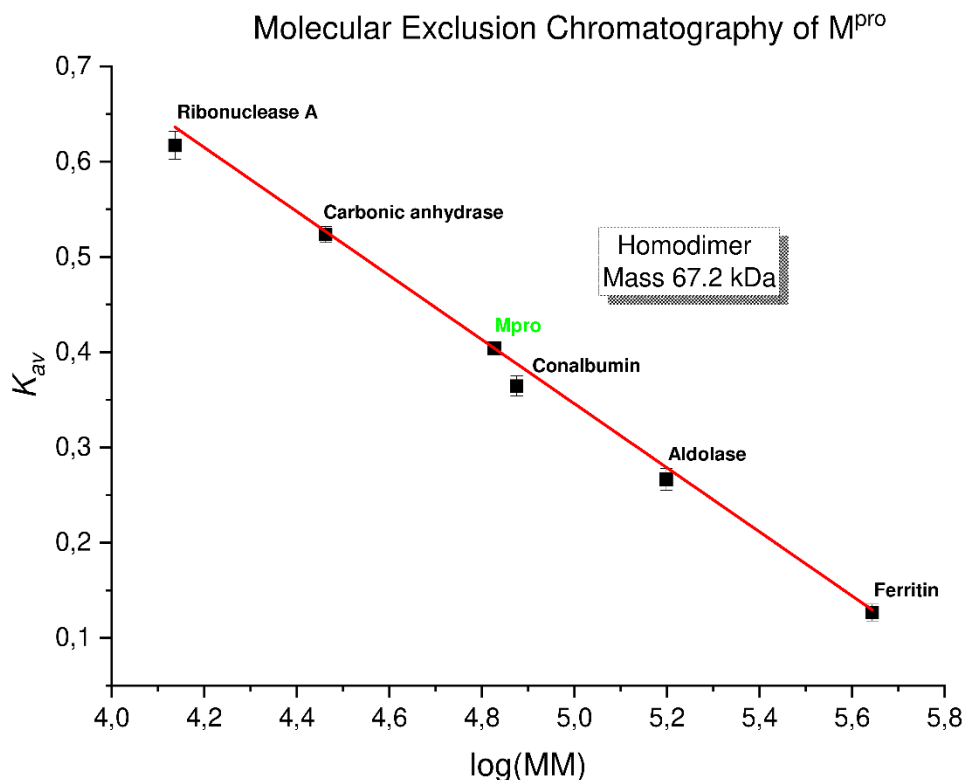
Figura 5. Eluição de M^{pro} em cromatografia de exclusão molecular. Foi utilizado coluna Superdex^{TM} Increase 200 10/300 GL (Cytiva, USA). O kit de calibração de filtração em gel LMW e HMW (Cytiva, USA) foi aplicado: Ferritina (440 kDa), Aldolase (158 kDa), Canalbumina (75 kDa), Anidrase Carbônica (29 kDa) e Ribonuclease (13,7 kDa). O K_{av} dos padrões e de M^{pro} foram representados graficamente em relação ao logarítimo de seus pesos moleculares. A massa molecular (MM) de M^{pro} foi calculado por ajuste linear. As corridas realizadas em modo isocrático com tampão fosfato 50 mM + NaCl 150 mM, pH 7,2 e à temperatura ambiente e fluxo de 0,5 mL/min. Os comprimentos de onda de 214 e 280 nm foram utilizados para monitorar a corrida. A MM estimada para M^{pro} em solução foi de 67,182 Da. Variáveis de equação linear: a = 2,02718; b = -0,33626; K_{av} (y) = 0,40397; R^2 = 0,99345.

### 3.3. Análise cinética dos compostos sintéticos e extratos de *Poincianella pluviosa*

A atividade enzimática de M^{pro} foi confirmada pela emissão de fluorescência causada pela hidrólise do substrato sintético (Figura 6). A Figura 6 mostra a curva de atividade enzimática pela concentração de substrato, onde foram verificadas as constantes K$_M$ de 34,58 ± 4,90 μM e V$_{máx}$ 51,33 ± 5,38 rFu/s usando a equação de Hill adaptada a Michaelis–Menten (Equação 3). Foi verificado que não há nenhuma informação cinética de M^{pro} com este substrato fluorogênico na plataforma Brenda Enzymes; assim, estes dados poderão se somar as informações já existentes de outros substratos neste banco de dados [51]. Também pode ser verificado na Figura 6 uma discreta tendência de formação de uma curva sigmóide, evidenciado pelo comportamento do ajuste não linear em baixas

concentrações de substrato fluorogênico, ao invés de um comportamento de hipérbole retangular característico de uma enzima michaeliana, indicando uma discreta cooperatividade. Este comportamento cooperativo pode ser evidenciado pelo n de 1,48 encontrado, apontando que após a ligação do substrato em um dos monômeros de M^{pro}, a afinidade do outro monômero pelo substrato aumenta.
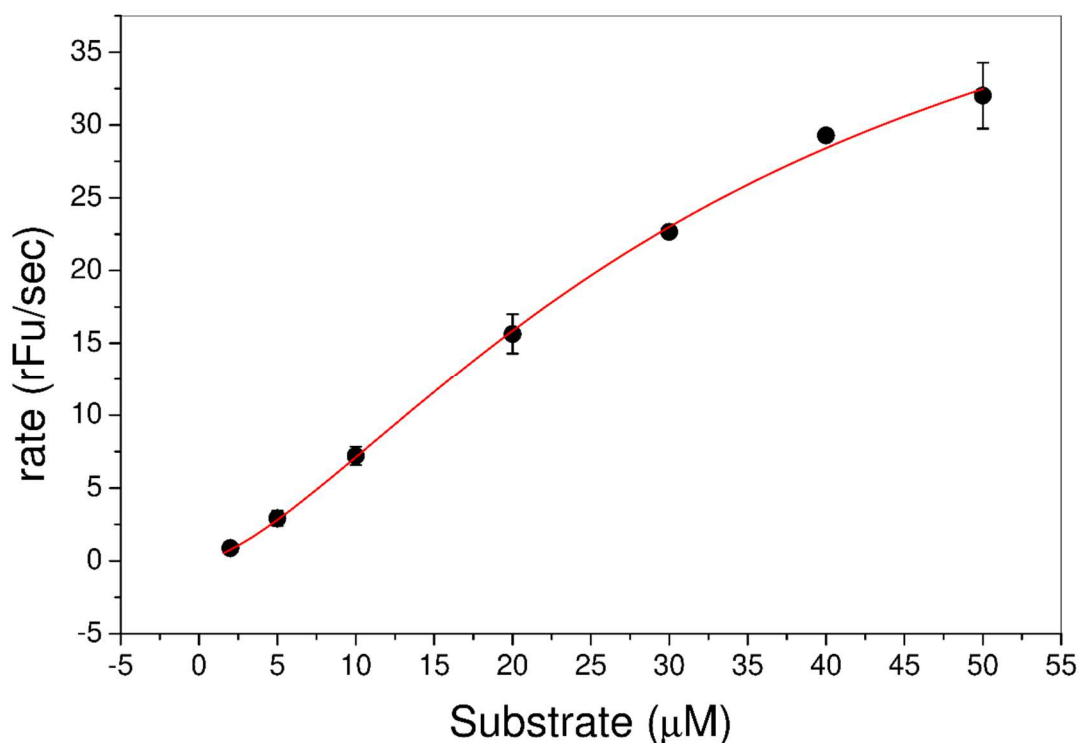
Figura 6. Atividade proteolítica de M^{pro} recombinante. Gráfico de Michaelis-Menten $R^2 = 0.998$. O tampão de reação foi o 50 mM Tris-HCl, pH 7.5, 1 mM EDTA. K_M de 34,58 ± 4,90 μM, V_{max} 51,33 rFu/s e n de 1,48 ± 0,14 A concentração da enzima foi de 1 μM e o substrato foi testado nas concentrações de 2, 5, 10, 20, 30, 40 e 50 μM.

A atividade inibitória dos 7 compostos foi avaliada em ponto único (Figura 7) e na mesma concentração, 43.8 μg.mL^{-1}. A amostra Controle 1 é a reação onde nem inibidor, nem DMSO foram adicionados, sendo a condição com menor interferência possível no estudo. No Controle 2, foi adicionado DMSO sozinho, sem adição de nenhum inibidor, para avaliar se poderia modificar a atividade de M^{pro}. Na Figura 7A nota-se a influência negativa causada pela adição de DMSO, mesmo em baixa concentração em relação ao volume total da reação (1.67%). Desta forma, a atividade de M^{pro} nos testes com os inibidores foi representada em relação à atividade encontrada no Controle 2; assim, as velocidades encontradas nos primeiros 60 s de reação para todos os compostos foram normalizadas em relação ao Controle 2 (Figura 7B).
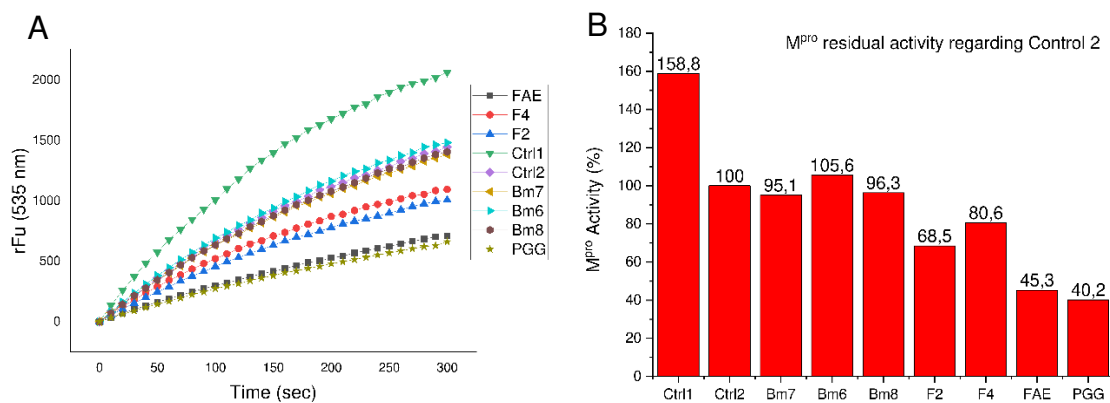
Figura 7. Avaliação da inibição da atividade proteolítica de M^{pro} causada pelos 7 compostos analisados. (**A**) Monitoramento dos 300 s do teste em 535 nm. (**B**) Atividade dos 7 compostos avaliados mais o Controle 1, normalizados em relação ao Controle 2. O tampão de reação foi o 50 mM Tris-HCl, pH 7.5, 1 mM EDTA. A concentração da enzima foi de 1 μM, substrato testado na concentrações de 10 μM e os composto em 43.8 μg.mL^{-1}.

O Controle 1 apresentou ~60% mais atividade que o Controle 2; mesmo em baixas concentrações, o DMSO foi capaz de diminuir a atividade hidrolítica de M^{pro}. A atividade enzimática é dependente do enovelamento adequado da proteína, sendo, este último, regido por um delicado equilíbrio entre as interações físico-químicas intrínsecas de uma proteína e seu ambiente que orientam sua estrutura e estabilidade. Como o DMSO é um co-solvente frequentemente utilizado para a solubilização de drogas hidrofóbicas, pois é miscível em água e na maioria dos líquidos orgânicos, assim, pode favorecer a exposição de resíduos hidrofóbicos alojados no interior da proteína ao ambiente, refletindo nas interações que estabilizam um polipeptídeo dobrado [52]. Na literatura é possível encontrar diversos trabalhos que apontam a capacidade do DMSO inibir a atividade de diversas enzimas, incluindo proteases, mesmo em baixas concentrações [53–56]. Nós descartamos a possibilidade da diminuição da atividade de M^{pro} ser causada pela absorção de luz fluorescente pelo DMSO, pois este é opticamente inerte nos comprimentos de onda analisados [57].

O composto que apresentou maior atividade inibitória foi o PGG, inibindo quase 60% da atividade de M^{pro}. Estes dados corroboram com os resultados encontrados nos experimentos *in sílico*, onde o PGG foi o composto melhor ranqueado nas análises de *docking*. Adicionalmente, também corrobora com este resultado o fato de o PGG estar isolado, não fazendo parte de um extrato. As frações FAE, F4 e F2 apresentaram, aproximadamente, 55, 20 e 32% de atividade inibitória, respectivamente. Em função

destes resultados, estas frações de *P. pluviosa* e o composto PGG isolado foram enviados para serem testados em células infectadas. Os compostos Bm6, Bm7 e Bm8 são substâncias sintéticas derivadas do produto natural Eugenol que se mostraram efetivos inibidores de protease do vírus West Nile [45]. Porém, estes compostos não apresentaram atividade inibitória sobre a M^{pro} e, por isso, não foram selecionados para ensaios em células Vero E6 infectadas.

3.4. Ensaios de citotoxicidade e atividade antiviral em células Vero E6

Os compostos que exibiram as melhores atividades inibitórias da proteína recombinante M^{pro} nas análises cinéticas foram submetidos ao teste com células Vero E6. Foi encontrado uma taxa de sobrevivência celular menor que 50% para os extratos de *P. pluviosa* (Figura 8A). O que apresentou menor toxicidade foi F4, com taxa de sobrevivência celular de 45,36% (Tabela 2). PGG foi o composto que apresentou maior taxa de sobrevivência celular, 55,23%.
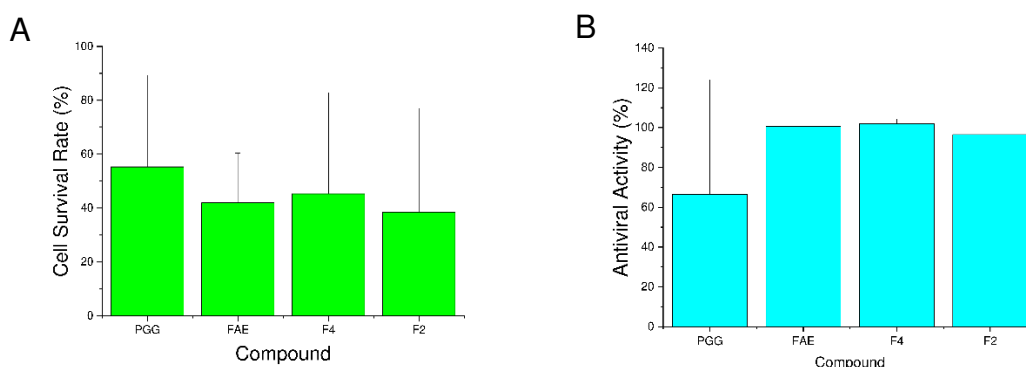
Figura 8. Análises de citotoxicidade e atividade antiviral em células Vero E6 em cultura. (**A**) Taxa de toxicidade celular dos quatro compostos analisados. (**B**) Atividade antiviral dos extratos de *Poincianella pluviosa* e do composto sintético PGG.

Os dados de citotoxicidade para as frações EtOAc de *P. pluviosa* encontrados nesse estudo contrastam com os já publicados. Adriani et al. (2021) utilizou a mesma fração EtOAc (FAE), ao qual, não foi capaz induzir hemólise significativa de eritrócitos humanos até a contração de 500 µg/mL (3% de hemólise), valor 5 vezes maior do que o utilizado em nossos ensaios, sendo verificada hemólise apenas em altas concentrações (1.000 µg/mL demonstrou 21,2% de hemólise) [58]. Neste mesmo trabalho, também não foi verificada nenhuma toxicidade em ensaios *in vivo* com larvas de *Galleria mellonella* em concentrações de FAE até 62,5 µg/mL/kg de larva e na dosagem máxima testada (1.000,0 µg/mL/kg) foi verificada uma taxa de mortalidade de 30% após 10 dias de

inoculação. Em nosso estudo, uma menor citotoxicidade é completamente plausível olhando o desvio padrão na Figura 8A, isto ocorre devido a certas replicatas terem apresentado taxas de sobrevivência celular bem acima da média.

Tabela 2. Médias das taxas de sobrevivência celular e atividades inibitórias com as frações EtOAc de *Poincianella pluviosa* e de PGG sintético em células Vero E6.

Composto	Atividade Antiviral (%)	Taxa de Sobrevivência Celular (%)
PGG	66.44	55.23
FAE	100.50	41.96
F4	101.83	45.36
F2	96.53	38.56

Todas as frações de Sibipiruna apresentaram elevadíssimas atividades antivirais (Figura 8B), todas maiores que 96%. A Tabela 2 mostra que o composto PGG, mesmo possuindo uma boa atividade inibitória da M^{pro} (66,44%), foi o pior ranqueado quanto à atividade antiviral. Com base nos testes com células infectadas, as frações FAE e F4 apresentaram os melhores equilíbrios entre atividade antiviral/citotoxicidade. Pelo fato destes compostos terem apresentado o máximo da atividade possível para o teste na concentração de 100 µg.mL^{-1}, futuros estudos com concentrações menores serão avaliados para analisar a melhor relação dose/resposta e identificar o EC$_{50}$.

4. Discussão

Taninos são polifenóis de grande relevância dentro dos produtos naturais e são definidos como o único grupo de metabólitos fenólicos de peso molecular relativamente alto (500 – 30.000 Da), tendo a capacidade de complexar fortemente com carboidratos e proteínas [59]. Acredita-se que os taninos podem exercer seus efeitos biológicos de duas maneiras diferentes: (1) inabsorvível como uma estrutura complexa, produzindo efeitos locais no trato gastrointestinal com ação antioxidante, antimicrobiano, antiviral, antimutagênico e efeitos antinutriente, ou (2) como taninos absorvíveis ou metabólitos absorvíveis oriundos da fermentação colônica de taninos, que podem produzir efeitos sistêmicos em vários órgãos [60].

Os extratos de *P. pluviosa* (fração EtOAc) utilizados neste trabalho já foram investigados anteriormente por Bueno et al. (2014) empregando espectrometria de massas

(ESI-MS/MS) e ressonância magnética nuclear (RMN) de C^{13} em estado sólido. Foi verificada a presença de diversos polifenóis e taninos hidrolisáveis, sendo confirmada a presença de três dos quatro compostos mais bem ranqueados como inibidores de M^{pro} nas análises *in silico*: PGG, Tellimagrandin II e 1,2,3,6-Tetragalloylglucose [37]. Estes resultados reforçam a nossa proposta de que os taninos presentes no extrato de *P. pluviosa* atuam como inibidores de protease principal de SARS-CoV-2, tendo participação na atividade antiviral observada nos estudos de células infectadas. Outros compostos com potencial ação inibitória contra M^{pro} (pirogalol) [61], RNA polimerase dependente de RNA (ácido gálico, ácido elágico, corilagin) e inibidores da interação Spike-ACE2 (corilagin, Tellimagrandin II, PGG e geraniin) também foram identificados nos extratos de Sibipiruna [62–68].

A presença dos diversos compostos no extrato de *P. pluviosa* explica o melhor desempenho deste em relação ao PGG isolado nos testes com células Vero E6 infectadas, indicando que pode ter ocorrido a ação sinérgica dos taninos. A ação dos taninos em diferentes enzimas alvo simultaneamente acentuou o efeito antiviral do extrato, o que corrobora com o valor de ~100% encontrado para FAE e F4. Existe também a possibilidade dos compostos agirem em enzimas da célula hospedeira, como a serino-protease TMPRSS2, em concordância com a ação dual do ácido tânico em M^{pro} e em TMPRSS2, que possui um importante papel no mecanismo de invasão celular por SARS-CoV-2 [31,69]. Adicionalmente, como o inóculo viral foi introduzido posteriormente aos extratos, pode ter acontecido o bloqueio da invasão celular pela inibição da ligação do domínio de ligação ao receptor (RBD) da proteína Spike de SARS-CoV-2 com o receptor celular ACE2 humano. A ligação de taninos a componentes do envelope viral também acontece no vírus influenza A, vírus parainfluenza, vírus herpes tipo 1 e 2 e hepatite A, resultando na inibição da fixação ao receptor, não ocorrendo penetração via membrana plasmática [70].

A rica composição de taninos hidrolisáveis nos extratos de Sibipiruna pode apresentar uma vantagem extra, podendo propiciar uma melhora no quadro inflamatório, devido à ação antioxidante e anti-inflamatória dos taninos, reduzindo a morbidade e a mortalidade dos casos de Covid-19, ocasionado pelo seu papel na manutenção da homeostase redox [32]. Outra vantagem dos extratos utilizados neste estudo é que são extraídos a partir de uma espécie de planta bastante comum no Brasil, principalmente na

região da Mata Atlântica e Pantanal, sendo também extensamente utilizada na arborização de cidades [71].

Os resultados aqui são promissores, pois demonstram substâncias capazes de inibir 100% da atividade viral. Além disso, este trabalho sugere algumas moléculas que podem servir de base para modificações químicas que possam levar a uma afinidade aumentada para a M^{pro} e/ou uma atividade antiviral mais destacada. Apesar dos resultados promissores, mais estudos de citotoxicidade, determinação de EC_{50} e CC_{50} (concentrações de compostos que reduzem a taxa de infecção e a sobrevivência celular em 50%, respectivamente), bem como estudos em modelo animal infectado precisam ser realizados para avaliar a aplicação do extrato de *P. pluviosa* contra a Covid-19.

5. Conclusão

Em resumo, os resultados apresentados neste estudo mostram que as frações do extrato de *Poincianella pluviosa* possuem uma potente atividade antiviral em células Vero E6 infectadas com SARS-CoV-2, sugerindo como mecanismo de ação a inibição de M^{pro}, além de outros diversos alvos virais e da célula hospedeira, como a inibição da invasão viral, denotando um possível efeito preventivo adicional. A ação sinérgica dos diversos polifenóis e taninos presentes nos extratos de Sibipiruna tem como efeito a potente ação antiviral. A proeminente ação antiviral dos compostos contidos nas frações EtOAc os caracteriza como bons prospectos a fármacos, o que pode ajudar no desenvolvimento de futuros novos inibidores frente à escassa terapêutica contra Covid-19.

Conflito de interesses

Os autores declaram que não existe conflito de interesses.

6. Referências Bibliográficas

[1]   P. Zhou, X.-L. Yang, X.-G. Wang, B. Hu, L. Zhang, W. Zhang, H.-R. Si, Y. Zhu, B. Li, C.-L. Huang, H.-D. Chen, J. Chen, Y. Luo, H. Guo, R.-D. Jiang, M.-Q. Liu, Y. Chen, X.-R. Shen, X. Wang, X.-S. Zheng, K. Zhao, Q.-J. Chen, F. Deng, L.-L. Liu, B. Yan, F.-X. Zhan, Y.-Y. Wang, G.-F. Xiao, Z.-L. Shi, A pneumonia outbreak associated with a new coronavirus of probable bat origin, Nature 2020 579:7798. 579 (2020) 270–273. https://doi.org/10.1038/s41586-020-2012-7.

[2]   F. Wu, S. Zhao, B. Yu, Y.-M. Chen, W. Wang, Z.-G. Song, Y. Hu, Z.-W. Tao, J.-H. Tian, Y.-Y. Pei, M.-L. Yuan, Y.-L. Zhang, F.-H. Dai, Y. Liu, Q.-M. Wang, J.-J. Zheng, L. Xu, E.C. Holmes, Y.-Z. Zhang, A new coronavirus associated with human respiratory disease in China, Nature 2020 579:7798. 579 (2020) 265–269. https://doi.org/10.1038/s41586-020-2008-3.

[3]   C. Huang, Y. Wang, X. Li, L. Ren, J. Zhao, Y. Hu, L. Zhang, G. Fan, J. Xu, X. Gu, Z. Cheng, T. Yu, J. Xia, Y. Wei, W. Wu, X. Xie, W. Yin, H. Li, M. Liu, Y. Xiao, H. Gao, L. Guo, J. Xie, G. Wang, R. Jiang, Z. Gao, Q. Jin, J. Wang, B. Cao, Clinical features of patients infected with 2019 novel coronavirus in Wuhan, China, Lancet (London, England). 395 (2020) 497. https://doi.org/10.1016/S0140-6736(20)30183-5.

[4]   L. Subissi, C.C. Posthuma, A. Collet, J.C. Zevenhoven-Dobbe, A.E. Gorbalenya, E. Decroly, E.J. Snijder, B. Canard, I. Imbert, One severe acute respiratory syndrome coronavirus protein complex integrates processive RNA polymerase and exonuclease activities, Proceedings of the National Academy of Sciences of the United States of America. 111 (2014) E3900–E3909. https://doi.org/10.1073/PNAS.1323705111/-/DCSUPPLEMENTAL.

[5]   A. Hegyi, J. Ziebuhr, Conservation of substrate specificities among coronavirus main proteases, Journal of General Virology. 83 (2002) 595–599. https://doi.org/10.1099/0022-1317-83-3-595/CITE/REFWORKS.

[6]   Q. Li, C. Kang, Progress in Developing Inhibitors of SARS-CoV-2 3C-Like Protease, Microorganisms. 8 (2020) 1–18. https://doi.org/10.3390/MICROORGANISMS8081250.

[7]   W. Dai, B. Zhang, X.M. Jiang, H. Su, J. Li, Y. Zhao, X. Xie, Z. Jin, J. Peng, F. Liu, C. Li, Y. Li, F. Bai, H. Wang, X. Cheng, X. Cen, S. Hu, X. Yang, J. Wang, X. Liu, G. Xiao, H. Jiang, Z. Rao, L.K. Zhang, Y. Xu, H. Yang, H. Liu, Structure-based design of antiviral drug candidates targeting the SARS-CoV-2 main protease, Science. 368 (2020) 1331–1335. https://doi.org/10.1126/SCIENCE.ABB4489/SUPPL_FILE/PAP.PDF.

[8]   T. Pillaiyar, M. Manickam, V. Namasivayam, Y. Hayashi, S.-H. Jung, An Overview of Severe Acute Respiratory Syndrome–Coronavirus (SARS-CoV) 3CL Protease Inhibitors: Peptidomimetics and Small Molecule Chemotherapy, Journal of Medicinal Chemistry. 59 (2016) 6595. https://doi.org/10.1021/ACS.JMEDCHEM.5B01461.

[9]   H. Yang, W. Xie, X. Xue, K. Yang, J. Ma, W. Liang, Q. Zhao, Z. Zhou, D. Pei, J. Ziebuhr, R. Hilgenfeld, Y.Y. Kwok, L. Wong, G. Gao, S. Chen, Z. Chen, D. Ma, M. Bartlam, Z. Rao, Design of Wide-Spectrum Inhibitors Targeting Coronavirus Main Proteases, PLOS Biology. 3 (2005) e324. https://doi.org/10.1371/JOURNAL.PBIO.0030324.

[10]   Y. Kim, H. Liu, A.C. Galasiti Kankanamalage, S. Weerasekara, D.H. Hua, W.C. Groutas, K.O. Chang, N.C. Pedersen, Reversal of the Progression of Fatal Coronavirus Infection in Cats by a Broad-Spectrum Coronavirus Protease Inhibitor, PLOS Pathogens. 12 (2016) e1005531. https://doi.org/10.1371/JOURNAL.PPAT.1005531.

[11]   L. Zhang, D. Lin, X. Sun, U. Curth, C. Drosten, L. Sauerhering, S. Becker, K. Rox, R. Hilgenfeld, Crystal structure of SARS-CoV-2 main protease provides a basis for

design of improved α-ketoamide inhibitors, Science. 368 (2020) 409–412. https://doi.org/10.1126/SCIENCE.ABB3405.

[12]   X. Xue, H. Yu, H. Yang, F. Xue, Z. Wu, W. Shen, J. Li, Z. Zhou, Y. Ding, Q. Zhao, X.C. Zhang, M. Liao, M. Bartlam, Z. Rao, Structures of Two Coronavirus Main Proteases: Implications for Substrate Binding and Antiviral Drug Design, Journal of Virology. 82 (2008) 2515–2527. https://doi.org/10.1128/JVI.02114-07.

[13]   Z. Ren, L. Yan, N. Zhang, Y. Guo, C. Yang, Z. Lou, Z. Rao, The newly emerged SARS-Like coronavirus HCoV-EMC also has an "Achilles' heel": current effective inhibitor targeting a 3C-like protease, Protein & Cell 2013 4:4. 4 (2013) 248–250. https://doi.org/10.1007/S13238-013-2841-3.

[14]   F. Wang, C. Chen, W. Tan, K. Yang, H. Yang, Structure of Main Protease from Human Coronavirus NL63: Insights for Wide Spectrum Anti-Coronavirus Drug Design, Scientific Reports 2016 6:1. 6 (2016) 1–12. https://doi.org/10.1038/srep22677.

[15]   Z. Jin, X. Du, Y. Xu, Y. Deng, M. Liu, Y. Zhao, B. Zhang, X. Li, L. Zhang, C. Peng, Y. Duan, J. Yu, L. Wang, K. Yang, F. Liu, R. Jiang, X. Yang, T. You, X. Liu, X. Yang, F. Bai, H. Liu, X. Liu, L.W. Guddat, W. Xu, G. Xiao, C. Qin, Z. Shi, H. Jiang, Z. Rao, H. Yang, Structure of Mpro from SARS-CoV-2 and discovery of its inhibitors, Nature 2020 582:7811. 582 (2020) 289–293. https://doi.org/10.1038/s41586-020-2223-y.

[16]   J. Tan, K.H.G. Verschueren, K. Anand, J. Shen, M. Yang, Y. Xu, Z. Rao, J. Bigalke, B. Heisen, J.R. Mesters, K. Chen, X. Shen, H. Jiang, R. Hilgenfeld, pH-dependent Conformational Flexibility of the SARS-CoV Main Proteinase (Mpro) Dimer: Molecular Dynamics Simulations and Multiple X-ray Structure Analyses, Journal of Molecular Biology. 354 (2005) 25. https://doi.org/10.1016/J.JMB.2005.09.012.

[17]   J. Shi, J. Song, The catalysis of the SARS 3C-like protease is under extensive regulation by its extra domain, The Febs Journal. 273 (2006) 1035. https://doi.org/10.1111/J.1742-4658.2006.05130.X.

[18]   D. Needle, G.T. Lountos, D.S. Waugh, Structures of the Middle East respiratory syndrome coronavirus 3C-like protease reveal insights into substrate specificity, Acta

Crystallographica Section D: Biological Crystallography. 71 (2015) 1102. https://doi.org/10.1107/S1399004715003521.

[19]   Z. Jin, X. Du, Y. Xu, Y. Deng, M. Liu, Y. Zhao, B. Zhang, X. Li, L. Zhang, C. Peng, Y. Duan, J. Yu, L. Wang, K. Yang, F. Liu, R. Jiang, X. Yang, T. You, X. Liu, X. Yang, F. Bai, H. Liu, X. Liu, L.W. Guddat, W. Xu, G. Xiao, C. Qin, Z. Shi, H. Jiang, Z. Rao, H. Yang, Structure of Mpro from SARS-CoV-2 and discovery of its inhibitors, Nature 2020 582:7811. 582 (2020) 289–293. https://doi.org/10.1038/s41586-020-2223-y.

[20]   C. Wu, Y. Liu, Y. Yang, P. Zhang, W. Zhong, Y. Wang, Q. Wang, Y. Xu, M. Li, X. Li, M. Zheng, L. Chen, H. Li, Analysis of therapeutic targets for SARS-CoV-2 and discovery of potential drugs by computational methods, Acta Pharmaceutica Sinica. B. 10 (2020) 766. https://doi.org/10.1016/J.APSB.2020.02.008.

[21]   W. Dai, B. Zhang, X.M. Jiang, H. Su, J. Li, Y. Zhao, X. Xie, Z. Jin, J. Peng, F. Liu, C. Li, Y. Li, F. Bai, H. Wang, X. Cheng, X. Cen, S. Hu, X. Yang, J. Wang, X. Liu, G. Xiao, H. Jiang, Z. Rao, L.K. Zhang, Y. Xu, H. Yang, H. Liu, Structure-based design of antiviral drug candidates targeting the SARS-CoV-2 main protease, Science. 368 (2020) 1331–1335. https://doi.org/10.1126/SCIENCE.ABB4489/SUPPL_FILE/PAP.PDF.

[22]   D. JA, G. HG, H. RW, Innovation in the pharmaceutical industry: New estimates of R&D costs, Journal of Health Economics. 47 (2016) 20–33. https://doi.org/10.1016/J.JHEALECO.2016.01.012.

[23]   Y. Wang, D. Zhang, G. Du, R. Du, J. Zhao, Y. Jin, S. Fu, L. Gao, Z. Cheng, Q. Lu, Y. Hu, G. Luo, K. Wang, Y. Lu, H. Li, S. Wang, S. Ruan, C. Yang, C. Mei, Y. Wang, D. Ding, F. Wu, X. Tang, X. Ye, Y. Ye, B. Liu, J. Yang, W. Yin, A. Wang, G. Fan, F. Zhou, Z. Liu, X. Gu, J. Xu, L. Shang, Y. Zhang, L. Cao, T. Guo, Y. Wan, H. Qin, Y. Jiang, T. Jaki, F.G. Hayden, P.W. Horby, B. Cao, C. Wang, Remdesivir in adults with severe COVID-19: a randomised, double-blind, placebo-controlled, multicentre trial, The Lancet. 395 (2020) 1569–1578. https://doi.org/10.1016/S0140-6736(20)31022-9/ATTACHMENT/9A4ED53E-D80B-42D4-9441-05DC6FC80E61/MMC1.PDF.

[24]   J.H. Beigel, K.M. Tomashek, L.E. Dodd, A.K. Mehta, B.S. Zingman, A.C. Kalil, E. Hohmann, H.Y. Chu, A. Luetkemeyer, S. Kline, D. Lopez de Castilla, R.W. Finberg, K. Dierberg, V. Tapson, L. Hsieh, T.F. Patterson, R. Paredes, D.A. Sweeney, W.R. Short, G. Touloumi, D.C. Lye, N. Ohmagari, M. Oh, G.M. Ruiz-Palacios, T. Benfield, G. Fätkenheuer, M.G. Kortepeter, R.L. Atmar, C.B. Creech, J. Lundgren, A.G. Babiker, S. Pett, J.D. Neaton, T.H. Burgess, T. Bonnett, M. Green, M. Makowski, A. Osinusi, S. Nayak, H.C. Lane, Remdesivir for the Treatment of Covid-19 — Final Report, New England Journal of Medicine. 383 (2020) 1813–1826. https://doi.org/10.1056/NEJMOA2007764/SUPPL_FILE/NEJMOA2007764_DATA-SHARING.PDF.

[25]   S. Ben-Shabat, L. Yarmolinsky, D. Porat, A. Dahan, Antiviral effect of phytochemicals from medicinal plants: Applications and drug delivery strategies, Drug Delivery and Translational Research. 10 (2020) 354. https://doi.org/10.1007/S13346-019-00691-6.

[26]   M.T. Islam, C. Sarkar, D.M. El-Kersh, S. Jamaddar, S.J. Uddin, J.A. Shilpi, M.S. Mubarak, Natural products and their derivatives against coronavirus: A review of the non-clinical and pre-clinical data, Phytotherapy Research. 34 (2020) 2471–2492. https://doi.org/10.1002/PTR.6700.

[27]   A. Pizzi, Tannins: Prospectives and Actual Industrial Applications, Biomolecules. 9 (2019). https://doi.org/10.3390/BIOM9080344.

[28]   K. Ueda, R. Kawabata, T. Irie, Y. Nakai, Y. Tohya, T. Sakaguchi, Inactivation of Pathogenic Viruses by Plant-Derived Tannins: Strong Effects of Extracts from Persimmon (Diospyros kaki) on a Broad Range of Viruses, PLoS ONE. 8 (2013) 55343. https://doi.org/10.1371/JOURNAL.PONE.0055343.

[29]   S. Espada, L. Faccin-Galhardi, V. Rincao, A. Bernardi, N. Lopes, R. Longhini, J. de Mello, R. Linhares, C. Nozawa, Antiviral Activity of Trichilia catigua Bark Extracts for Herpesvirus and Poliovirus, Current Pharmaceutical Biotechnology. 16 (2015) 724–732. https://doi.org/10.2174/1389201016666150505125235.

[30]   A.M.M. Felipe, V.P. Rincão, F.J. Benati, R.E.C. Linhares, K.J. Galina, C.E.M. de Toledo, G.C. Lopes, J.C.P. de Mello, C. Nozawa, Antiviral Effect of Guazuma ulmifolia and Stryphnodendron adstringens on Poliovirus and Bovine Herpesvirus, Biological and Pharmaceutical Bulletin. 29 (2006) 1092–1095. https://doi.org/10.1248/BPB.29.1092.

[31]   S.-C. Wang, Y. Chen, Y.-C. Wang, W.-J. Wang, C.-S. Yang, C.-L. Tsai, M.-H. Hou, H.-F. Chen, Y.-C. Shen, M.-C. Hung, Tannic acid suppresses SARS-CoV-2 as a dual inhibitor of the viral main protease and the cellular TMPRSS2 protease, American Journal of Cancer Research. 10 (2020) 4538. /pmc/articles/PMC7783773/ (accessed September 1, 2021).

[32]   M. Goli, Review of novel human β-coronavirus (2019-nCoV or SARS-CoV-2) from the food industry perspective—Appropriate approaches to food production technology, Food Science & Nutrition. 8 (2020) 5228. https://doi.org/10.1002/FSN3.1892.

[33]   Mesecar, Andrew D., A taxonomically-driven approach to development of potent, broad-spectrum inhibitors of coronavirus main protease including SARS-CoV-2 (COVID-19), (2020).

[34]   O. Trott, A.J. Olson, AutoDock Vina: improving the speed and accuracy of docking with a new scoring function, efficient optimization and multithreading, Journal of Computational Chemistry. 31 (2010) 455. https://doi.org/10.1002/JCC.21334.

[35]   A.K. Rappe, C.J. Casewit, K.S. Colwell, W.A.G. III, W.M. Skiff, UFF, a full periodic table force field for molecular mechanics and molecular dynamics simulations, Journal of the American Chemical Society. 114 (2002) 10024–10035. https://doi.org/10.1021/JA00051A040.

[36]   G. Bitencourt-Ferreira, W.F. de Azevedo, Molegro Virtual Docker for Docking, Methods in Molecular Biology. 2053 (2019) 149–167. https://doi.org/10.1007/978-1-4939-9752-7_10.

[37]   F.G. Bueno, G.P. Panizzon, E.V.S.D.L. Mello, M. Lechtenberg, F. Petereit, J.C.P. de Mello, A. Hensel, Hydrolyzable tannins from hydroalcoholic extract from Poincianella pluviosa stem bark and its wound-healing properties: Phytochemical investigations and

influence on in vitro cell physiology of human keratinocytes and dermal fibroblasts, Fitoterapia. 99 (2014) 252–260. https://doi.org/10.1016/J.FITOTE.2014.10.007.

[38]   T. Sterling, J.J. Irwin, ZINC 15 – Ligand Discovery for Everyone, Journal of Chemical Information and Modeling. 55 (2015) 2324. https://doi.org/10.1021/ACS.JCIM.5B00559.

[39]   Y. Wang, J. Xiao, T.O. Suzek, J. Zhang, J. Wang, S.H. Bryant, PubChem: a public information system for analyzing bioactivities of small molecules, Nucleic Acids Research. 37 (2009) W623. https://doi.org/10.1093/NAR/GKP456.

[40]   N.M. O'Boyle, M. Banck, C.A. James, C. Morley, T. Vandermeersch, G.R. Hutchison, Open Babel: An open chemical toolbox, Journal of Cheminformatics 2011 3:1. 3 (2011) 1–14. https://doi.org/10.1186/1758-2946-3-33.

[41]   Molecular Cloning: A Laboratory Manual, 3rd ed., Vols 1,2 and 3 J.F. Sambrook and D.W. Russell, ed., Cold Spring Harbor Laboratory Press, 2001, 2100 pp., soft cover, (n.d.).

[42]   M.R. Wilkins, E. Gasteiger, A. Bairoch, J.C. Sanchez, K.L. Williams, R.D. Appel, D.F. Hochstrasser, Protein identification and analysis tools in the ExPASy server., Methods in Molecular Biology (Clifton, N.J.). 112 (1999) 531–552. https://doi.org/10.1385/1-59259-584-7:531.

[43]   S.P. Leytus, W.L. Patterson, W.F. Mangel, New class of sensitive and selective fluorogenic substrates for serine proteinases. Amino acid and dipeptide derivatives of rhodamine., Biochemical Journal. 215 (1983) 253. https://doi.org/10.1042/BJ2150253.

[44]   S.P. Leytus, L.L. Melhado, W.F. Mangel, Rhodamine-based compounds as fluorogenic substrates for serine proteinases., Biochemical Journal. 209 (1983) 299. https://doi.org/10.1042/BJ2090299.

[45]   A.S. de Oliveira, P.A.R. Gazolla, A.F.C.S. da Oliveira, W.L. Pereira, L.C.S. de Viol, A.F.S. da Maia, E.G. Santos, Í.E.P. da Silva, T.A. de Oliveira Mendes, A.M. da Silva, R.S. Dias, C.C. da Silva, M.D. Polêto, R.R. Teixeira, S.O. de Paula, Discovery of novel West Nile Virus protease inhibitor based on isobenzonafuranone and triazolic

derivatives of eugenol and indan-1,3-dione scaffolds, PLoS ONE. 14 (2019). https://doi.org/10.1371/JOURNAL.PONE.0223017.

[46]   A.E. Gorbalenya, E.J. Snijder, Viral cysteine proteinases, Perspectives in Drug Discovery and Design. 6 (1996) 64. https://doi.org/10.1007/BF02174046.

[47]   N. Neamati, H. Hong, A. Mazumder, S. Wang, S. Sunder, M.C. Nicklaus, G.W.A. Milne, B. Proksa, Y. Pommier, Depsides and Depsidones as Inhibitors of HIV-1 Integrase: Discovery of Novel Inhibitors through 3D Database Searching†, Journal of Medicinal Chemistry. 40 (1997) 942–951. https://doi.org/10.1021/JM960759E.

[48]   T.H. Vu, A.C. le Lamer, C. Lalli, J.B.M. Samson, F.L. le Dévéhat, J. le Seyec, Depsides: Lichen Metabolites Active against Hepatitis C Virus, PLOS ONE. 10 (2015) e0120405. https://doi.org/10.1371/JOURNAL.PONE.0120405.

[49]   C.G. Kato-Schwartz, F. Bracht, G. de A. Gonçalves, A.A. Soares, T.F. Vieira, T. Brugnari, A. Bracht, R.M. Peralta, Inhibition of α-amylases by pentagalloyl glucose: Kinetics, molecular dynamics and consequences for starch absorption, Journal of Functional Foods. 44 (2018) 265–273. https://doi.org/10.1016/J.JFF.2018.03.025.

[50]   L. Li, A.A. Shaik, J. Zhang, K. Nhkata, L. Wang, Y. Zhang, C. Xing, S.H. Kim, J. Lü, Preparation of Penta-O-galloyl-β-D-glucose from tannic acid and plasma pharmacokinetic Analyses by Liquid-Liquid Extraction and Reverse-Phase HPLC, Journal of Pharmaceutical and Biomedical Analysis. 54 (2011) 545. https://doi.org/10.1016/J.JPBA.2010.09.028.

[51]   I. Schomburg, A. Chang, O. Hofmann, C. Ebeling, F. Ehrentreich, D. Schomburg, BRENDA: a resource for enzyme data and metabolic information, Trends in Biochemical Sciences. 27 (2002) 54–56. https://doi.org/10.1016/S0968-0004(01)02027-8.

[52]   J.J. Modrzyński, J.H. Christensen, K.K. Brandt, Evaluation of dimethyl sulfoxide (DMSO) as a co-solvent for toxicity testing of hydrophobic organic compounds, Ecotoxicology. 28 (2019) 1136–1141. https://doi.org/10.1007/S10646-019-02107-0/TABLES/1.

[53]   S. Wang, X. Meng, H. Zhou, Y. Liu, F. Secundo, Y. Liu, Enzyme Stability and Activity in Non-Aqueous Reaction Systems: A Mini Review, Catalysts 2016, Vol. 6, Page 32. 6 (2016) 32. https://doi.org/10.3390/CATAL6020032.

[54]   C. Qiao, H. Yanfei, L. Jinhua, C. Qingxi, Effect of dimethyl sulfxide (DMSO) on activity and conformation of alkaline phosphatase from Haliotis diversicolor, Xiamen Da Xue Xue Bao. Zi Ran Ke Xue Ban = Journal of Xiamen University. Natural Science. 44 (2005) 836–838. https://europepmc.org/article/cba/604817 (accessed August 31, 2021).

[55]   L. Misuri, M. Cappiello, F. Balestri, R. Moschini, V. Barracco, U. Mura, A. Del-Corso, The use of dimethylsulfoxide as a solvent in enzyme inhibition studies: the case of aldose reductase, Journal of Enzyme Inhibition and Medicinal Chemistry. 32 (2017) 1152. https://doi.org/10.1080/14756366.2017.1363744.

[56]   A. Kumar, T. Darreh-Shori, DMSO: A Mixed-Competitive Inhibitor of Human Acetylcholinesterase, ACS Chemical Neuroscience. 8 (2017) 2618–2625. https://doi.org/10.1021/ACSCHEMNEURO.7B00344.

[57]   C. Marcovicz, R.C. Ferreira, A.B.S. Santos, A.S. Reyna, C.B. de Araújo, I. Malvestiti, E.H.L. Falcão, Nonlinear optical behavior of two tetrathiafulvalene derivatives in the picosecond regime, Chemical Physics Letters. 702 (2018) 16–20. https://doi.org/10.1016/J.CPLETT.2018.04.053.

[58]   G.M. Andriani, A.E.B. Morguette, L.F.A. Spoladori, P.M.L. Pereira, W.R.C. Cabral, B.T. Fernandes, E.R. Tavares, R.S. Almeida, C.A.C. Lancheros, C.V. Nakamura, J.C.P. Mello, L.M. Yamauchi, S.F. Yamada-Ogatta, Antifungal Combination of Ethyl Acetate Extract of Poincianella pluviosa (DC.) L. P. Queiros Stem Bark With Amphotericin B in Cryptococcus neoformans, Frontiers in Microbiology. 0 (2021) 1383. https://doi.org/10.3389/FMICB.2021.660645.

[59]   J. Serrano, R. Puupponen-Pimiä, A. Dauer, A.M. Aura, F. Saura-Calixto, Tannins: Current knowledge of food sources, intake, bioavailability and biological effects, Molecular Nutrition & Food Research. 53 (2009) S310–S329. https://doi.org/10.1002/MNFR.200900039.

[60] E, Haslam, Natural polyphenols (vegetable tannins) as drugs: possible modes of action., Journal of Natural Products. 59 (1996) 205–215. https://doi.org/10.1021/np960040+.

[61] H. Su, S. Yao, W. Zhao, Y. Zhang, J. Liu, Q. Shao, Q. Wang, M. Li, H. Xie, W. Shang, C. Ke, L. Feng, X. Jiang, J. Shen, G. Xiao, H. Jiang, L. Zhang, Y. Ye, Y. Xu, Identification of pyrogallol as a warhead in design of covalent inhibitors for the SARS-CoV-2 3CL protease, Nature Communications. 12 (2021). https://doi.org/10.1038/S41467-021-23751-3.

[62] N. El-Aziz, M. Shehata, O. Awad, S. El-Sohaimy, Inhibition of COVID-19 RNA-Dependent RNA Polymerase by Natural Bioactive Compounds: Molecular Docking Analysis, (2020). https://doi.org/10.21203/RS.3.RS-25850/V1.

[63] A. ben David, E. Diamant, E. Dor, A. Barnea, N. Natan, L. Levin, S. Chapman, L.C. Mimran, E. Epstein, R. Zichel, A. Torgeman, Identification of SARS-CoV-2 Receptor Binding Inhibitors by In Vitro Screening of Drug Libraries, Molecules. 26 (2021). https://doi.org/10.3390/MOLECULES26113213.

[64] Q. Li, D. Yi, X. Lei, J. Zhao, Y. Zhang, X. Cui, X. Xiao, T. Jiao, X. Dong, X. Zhao, H. Zeng, C. Liang, L. Ren, F. Guo, X. Li, J. Wang, S. Cen, Corilagin inhibits SARS-CoV-2 replication by targeting viral RNA-dependent RNA polymerase, Acta Pharmaceutica Sinica B. 11 (2021) 1555–1567. https://doi.org/10.1016/J.APSB.2021.02.011.

[65] L.J. Yang, R.H. Chen, S. Hamdoun, P. Coghi, J.P.L. Ng, D.W. Zhang, X. Guo, C. Xia, B.Y.K. Law, V.K.W. Wong, Corilagin prevents SARS-CoV-2 infection by targeting RBD-ACE2 binding, Phytomedicine. 87 (2021) 153591. https://doi.org/10.1016/J.PHYMED.2021.153591.

[66] V. Umashankar, S.H. Deshpande, H. v. Hegde, I. Singh, D. Chattopadhyay, Phytochemical Moieties From Indian Traditional Medicine for Targeting Dual Hotspots on SARS-CoV-2 Spike Protein: An Integrative in-silico Approach, Frontiers in Medicine. 8 (2021) 672629. https://doi.org/10.3389/FMED.2021.672629.

[67]   R.H. Chen, L.J. Yang, S. Hamdoun, S.K. Chung, C.W. Lam, K.X. Zhang, X. Guo, C. Xia, B.Y.K. Law, V.K.W. Wong, 1,2,3,4,6-Pentagalloyl Glucose, a RBD-ACE2 Binding Inhibitor to Prevent SARS-CoV-2 Infection, Frontiers in Pharmacology. 0 (2021) 150. https://doi.org/10.3389/FPHAR.2021.634176.

[68]   Y.S. Kim, H.-S. Chung, S.G. Noh, B. Lee, H.Y. Chung, J.-G. Choi, Geraniin Inhibits the Entry of SARS-CoV-2 by Blocking the Interaction between Spike Protein RBD and Human ACE2 Receptor, International Journal of Molecular Sciences. 22 (2021). https://doi.org/10.3390/IJMS22168604.

[69]   M. Scudellari, HOW THE CORONAVIRUS INFECTS OUR CELLS Scientists are unpicking SARS-CoV-2's life cycle, | Nature |. 595 (2021).

[70]   R. Ubillas, S.D. Jolad, R.C. Bruening, M.R. Kernan, S.R. King, D.F. Sesin, M. Barrett, C.A. Stoddart, T. Flaster, J. Kuo, F. Ayala, E. Meza, M. Castañel, D. Mcmeekin, E. Rozhon, M.S. Tempesta, D. Barnard, J. Huffman, D. Smee, R. Sidwell, K. Soike, A. Brazier, S. Safrin, R. Orlando, P.T.M. Kenny, N. Berova, K. Nakanishi, SP-303, an antiviral oligomeric proanthocyanidin from the latex of Croton lechleri (Sangre de Drago)., Phytomedicine. 1 (1994) 77–106. https://doi.org/10.1016/S0944-7113(11)80026-7.

[71]   C.A. Pontes, V.B. Corte, E.E. de L. e Borges, A.G. da Silva, R. de C.G. Borges, Influência da temperatura de armazenamento na qualidade das sementes de Caesalpinia peltophoroides Benth. (sibipiruna), Revista Árvore. 30 (2006) 43–48. https://doi.org/10.1590/S0100-67622006000100006.

Trabalhos Publicados na Vigência do Doutorado

Taylor & Francis
Taylor & Francis Group

RESEARCH PAPER

Check for updates

Identification and characterization of stem-bulge RNAs in *Drosophila melanogaster*

Francisco Ferreira Duarte Junior[a], Paulo Sérgio Alves Bueno[b], Sofia L. Pedersen[c], Fabiana dos Santos Rando[d], José Renato Pattaro Júnior[b], Daniel Caligari[a], Anelise Cardoso Ramos[a], Lorena Gomes Polizelli[a], Ailson Francisco dos Santos Lima[a], Quirino Alves de Lima Neto [a], Torsten Krude [c], Flavio Augusto Vicente Seixas [b], and Maria Aparecida Fernandez [a]

[a]Departamento de Biotecnologia, Genética e Biologia Celular, Universidade Estadual de Maringá, Maringá, Paraná, Brazil; [b]Departamento de Tecnologia, Universidade Estadual de Maringá, campus Umuarama, Umuarama, Paraná, Brazil; [c]Department of Zoology, University of Cambridge, Cambridge, UK; [d]Center for Molecular, Structural and Functional Biology - CBM/COMCAP, Universidade Estadual de Maringá, Maringá, Paraná, Brazil

ABSTRACT

Non-coding Y RNAs and stem-bulge RNAs are homologous small RNAs in vertebrates and nematodes, respectively. They share a conserved function in the replication of chromosomal DNA in these two groups of organisms. However, functional homologues have not been found in insects, despite their common early evolutionary history. Here, we describe the identification and functional characterization of two sbRNAs in *Drosophila melanogaster*, termed Dm1 and Dm2. The genes coding for these two RNAs were identified by a computational search in the genome of *D. melanogaster* for conserved sequence motifs present in nematode sbRNAs. The predicted secondary structures of Dm1 and Dm2 partially resemble nematode sbRNAs and show stability in molecular dynamics simulations. Both RNAs are phylogenetically closer related to nematode sbRNAs than to vertebrate Y RNAs. Dm1, but not Dm2 sbRNA is abundantly expressed in *D. melanogaster* S2 cells and adult flies. Only Dm1, but not Dm2 sbRNA can functionally replace Y RNAs in a human cell-free DNA replication initiation system. Therefore, Dm1 is the first functional sbRNA described in insects, allowing future investigations into the physiological roles of sbRNAs in the genetically tractable model organism *D. melanogaster*.

Introduction

Non-coding RNAs (ncRNAs) regulate many fundamental pathways in eukaryotic organisms. Two families of ncRNAs play essential functional roles during chromosomal DNA replication: Y RNAs in vertebrates and stem-bulge RNAs (sbRNAs) in nematodes [1,2]. Y RNAs have been shown to be essential for the initiation of chromosomal DNA replication in a human cell-free system, for DNA replication and cell proliferation in cultured vertebrate cells and for early development and viability of *Xenopus laevis* and the zebrafish, *Danio rerio* [3–5]. sbRNAs are able to functionally replace endogenous Y RNAs in a human DNA replication initiation system. They are also essential for DNA replication and cell proliferation in the nematode *Caenorhabditis elegans*, as well as its development and viability [6].

Both Y and sbRNAs show homology in function and structure [1,2,7,8]. Structurally, they comprise short stem-loop RNAs of around a hundred nucleotides in length. The partially complementary 5′ and 3′ ends hybridize to form a double-stranded stem structure with a central single-stranded loop. Common to both Y and sbRNAs are conserved nucleotide sequence elements in the stem structure. They comprise a short helix of 7–10 base pairs flanked by G-C base pairs either end, and a highly conserved double-

stranded GUG-CAC tri-nucleotide motif near the center of this domain. This domain is located in the upper stem of both ncRNA families, which opens up into the central loop domain. Importantly, these conserved motifs are essential for the function of these RNAs during the initiation of chromosomal DNA replication in a cell-free system because mutations in these elements abrogate their function [3,6,9,10].

Despite the similarities, there are a few differences between Y and sbRNAs. On the one hand, vertebrate Y RNAs contain a second helical motif with a bulged C residue towards the terminus of the stem-loop, which bind orthologues of the Ro60 protein. In fact, Y RNAs were originally described as the RNA component of Ro-ribonucleotide particles (Ro-RNPs), based on their association with Ro60 [11]. However, neither the Ro-binding domain nor the Ro60 protein are essential for Y RNA function during DNA replication [3,9,12], and they are not found in sbRNAs [1,2,6]. On the other hand, sbRNAs contain a highly conserved UUAUC penta-nucleotide motif at the 5′ end of the central single-stranded domain, which appears to play an additional stimulatory role for DNA replication [1,2,6].

In evolutionary terms, functional Y RNAs are found in all vertebrates investigated so far, and sbRNAs in several nematodes including *C. elegans* and *Caenorhabditis briggsae*

Biophysical characterization and molecular phylogeny of human KIN protein

José Renato Pattaro Júnior[1] · Ícaro Putinhon Caruso[2] · Quirino Alves de Lima Neto[3] ·
Francisco Ferreira Duarte Junior[3] · Fabiana dos Santos Rando[4] · Edileusa Cristina Marques Gerhardt[5] ·
Maria Aparecida Fernandez[3] · Flávio Augusto Vicente Seixas[1]

Abstract

The DNA/RNA-binding KIN protein was discovered in 1989, and since then, it has been found to participate in several processes, e.g., as a transcription factor in bacteria, yeasts, and plants, in immunoglobulin isotype switching, and in the repair and resolution of double-strand breaks caused by ionizing radiation. However, the complete three-dimensional structure and biophysical properties of KIN remain important information for clarifying its function and to help elucidate mechanisms associated with it not yet completely understood. The present study provides data on phylogenetic analyses of the different domains, as well as a biophysical characterization of the human KIN protein ($_{HSA}$KIN) using bioinformatics techniques, circular dichroism spectroscopy, and differential scanning calorimetry to estimate the composition of secondary structure elements; further studies were performed to determine the biophysical parameters ΔH_m and T_m. The phylogenetic analysis indicated that the zinc-finger and winged helix domains are highly conserved in KIN, with mean identity of 90.37% and 65.36%, respectively. The KOW motif was conserved only among the higher eukaryotes, indicating that this motif emerged later on the evolutionary timescale. $_{HSA}$KIN has more than 50% of its secondary structure composed by random coil and β-turns. The highest values of ΔH_m and T_m were found at pH 7.4 suggesting a stable structure at physiological conditions. The characteristics found for $_{HSA}$KIN are primarily due to its relatively low composition of α-helices and β-strands, making up less than half of the protein structure.

✉ Flávio Augusto Vicente Seixas
favseixas@uem.br

1 Department of Technology, Universidade Estadual de Maringá-UEM, Av. Ângelo Moreira da Fonseca, 1800, Umuarama, PR 87506-370, Brazil

2 Department of Physics, Instituto de Biociências, Letras e Ciências Exatas-Universidade Estadual Paulista "Júlio de Mesquita Filho", São José do Rio Preto, SP, Brazil

3 Department of Biotechnology, Genetics and Cell Biology, Universidade Estadual de Maringá, Maringá, PR, Brazil

4 Center for Molecular, Structural and Functional Biology, CBM-Research Support Center Complex, Universidade Estadual de Maringá, Maringá, PR, Brazil

5 Department of Biochemistry, Universidade Federal do Paraná, Curitiba, PR, Brazil

Introduction

Cell metabolism is composed of an intricate network of physical and biochemical processes, many of which depend on interactions between proteins and nucleic acids. The KIN protein is one of these proteins for which an interaction with nucleic acids has been proposed (le Maire et al. 2006b; Mazin et al. 1994a, b; Pinon-Lataillade et al. 2004). However, the mechanism of this interaction and the metabolic function of KIN have not yet been elucidated. KIN was identified in 1989 in Fisher's rat fibroblasts (FR 3T3) from the cross-reaction of monospecific polyclonal antibodies directed against the RecA protein from *Escherichia coli* (Angulo et al. 1989).

KIN is ubiquitously expressed in mammals and shows high expression in human skeletal muscle cells, heart, testis, and cells with high proliferation rates, including several tumor cell types (Ramos et al. 2015; Zhang et al. 2017a,

🖄 Springer

Purification and characterization of embryo-specific soy urease (*Glycine max*) and its antifungal potential against *Paracoccidioides brasiliensis*

Elisângela Andrade Ângelo[1], Tainá Michelle da Cruz[2], José Renato Pattaro Júnior[2], Daniele Maria Zanzarin[3], Franciele Abigail Vilugron Rodrigues[4], Eduardo Jorge Pilau[3], Érika Seki Kioshima[4], Maria Aparecida Fernandez[5], Flavio Augusto Vicente Seixas[2+]

1. Federal Institute of Paraná, Biology laboratory, Umuarama, Brazil.
2. State University of Maringá, Departament of Technology, Umuarama, Brazil.
3. State University of Maringá, Department of Chemistry, Maringá, Brazil.
4. State University of Maringá, Department of Clinical Analysis and Biotechnology, Maringá, Brazil.
5. State University of Maringá, Department of Biotechnology, Genetics and Cell Biology, Maringá, Brazil.

+Corresponding author: Flavio Augusto Vicente Seixas, Phone: +55 44 3621-9300, Email address: favseixas@uem.br

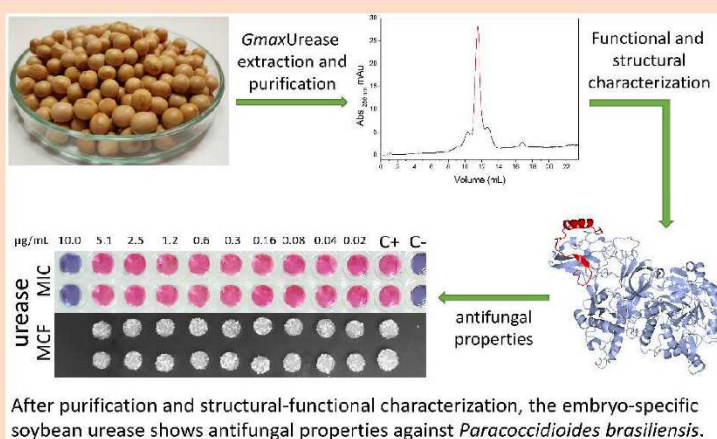**ABSTRACT:** Ureases are amidohydrolases that catalyze the hydrolysis of urea to ammonia and carbamate. In addition to the enzymatic function, ureases have fungitoxic and insecticidal function, which are independent of their catalytic activity. Soy (*Glycine max*) has two main urease isoforms: ubiquitous and embryo-specific, the latter is present in beans. In view of the potential applications of ureases, this work aimed to extract, purify, characterize the structure, activity and fungitoxic activity of soy urease against *Paracoccidioides brasiliensis*. The biochemical characterization was performed, in terms of optimal pH and temperature, as well as the determination of the Michaelis–Menten constant (K_M) and maximum velocity (V_{max}). The protein sequence was identified by mass spectrometry and used in computational modeling of the biological structure. The optimum pH and temperature of the enzyme were 6.5 and 65 °C, respectively, K_M 526 mmol L^{-1} and V_{max} 7.4 mmol L^{-1} NH3·μg_{urease}^{-1}·s^{-1} and biological unity as a trimer. The antifungal activity assays (*in vitro*) were promising, showing a fungicidal profile of the urease, with a minimum inhibitory concentration of 10 µg·mL^{-1}. This work demonstrated, for the first time, the fungitoxic activity of embryo-specific soy urease against the Pb18 strain of *P. brasiliensis*.

GmaxUrease extraction and purification → *Functional and structural characterization* → *antifungal properties*

After purification and structural-functional characterization, the embryo-specific soybean urease shows antifungal properties against *Paracoccidioides brasiliensis*.

Article

Interactome Analysis of KIN (Kin17) Shows New Functions of This Protein

Vanessa Pinatto Gaspar [1,2], Anelise Cardoso Ramos [1], Philippe Cloutier [2], José Renato Pattaro Junior [3], Francisco Ferreira Duarte Junior [1], Annie Bouchard [2], Flavio Augusto Vicente Seixas [3], Benoit Coulombe [2] and Maria Aparecida Fernandez [1,*]

[1] Departamento de Biotecnologia, Genética e Biologia Celular, Universidade Estadual de Maringá, Av. Colombo, 5790, Maringá 87020-900, Brazil; vapigas@gmail.com (V.P.G.); anelise.andre@gmail.com (A.C.R.); junior.fduarte@gmail.com (F.F.D.J.)

[2] Institut de Recherches Cliniques de Montréal, 110 Avenue des Pins Ouest, Montreal, QC H2W 1R7, Canada; phil.clou@gmail.com (P.C.); anniebouchard78@gmail.com (A.B.); benoit.coulombe@ircm.qc.ca (B.C.)

[3] Departamento de Tecnologia, Campus Umuarama, Universidade Estadual de Maringá, Av. Ângelo Moreira da Fonseca, 1800, Umuarama 87506-370, Brazil; pattoze@gmail.com (J.R.P.J.); favseixas@gmail.com (F.A.V.S.)

* Correspondence: mafernandez@uem.br; Tel.: +55-4430115398

Abstract: KIN (Kin17) protein is overexpressed in a number of cancerous cell lines, and is therefore considered a possible cancer biomarker. It is a well-conserved protein across eukaryotes and is ubiquitously expressed in all cell types studied, suggesting an important role in the maintenance of basic cellular function which is yet to be well determined. Early studies on KIN suggested that this nuclear protein plays a role in cellular mechanisms such as DNA replication and/or repair; however, its association with chromatin depends on its methylation state. In order to provide a better understanding of the cellular role of this protein, we investigated its interactome by proximity-dependent biotin identification coupled to mass spectrometry (BioID-MS), used for identification of protein–protein interactions. Our analyses detected interaction with a novel set of proteins and reinforced previous observations linking KIN to factors involved in RNA processing, notably pre-mRNA splicing and ribosome biogenesis. However, little evidence supports that this protein is directly coupled to DNA replication and/or repair processes, as previously suggested. Furthermore, a novel interaction was observed with PRMT7 (protein arginine methyltransferase 7) and we demonstrated that KIN is modified by this enzyme. This interactome analysis indicates that KIN is associated with several cell metabolism functions, and shows for the first time an association with ribosome biogenesis, suggesting that KIN is likely a moonlight protein.

Keywords: KIN (Kin17); cancer biomarker; protein–protein interactions; BioID-MS; splicing process; ribosome biogenesis

1. Introduction

KIN is described as a potential diagnostic biomarker and a potential target for breast cancer therapy [1,2], as well as a suitable marker for predicting chemotherapy response in colorectal carcinoma [3]. A study recently performed and published by our group demonstrated that KIN is differently expressed in subpopulations of melanoma from murine cell lines, according to its aggressiveness [4]. Studies of KIN in human colorectal cancer cells, using siRNA to silence its expression, indicated reduced cell proliferation and an accumulation of cells in the beginning or middle of cell cycle S phase [5]. KIN is overexpressed in most cancer cells studied so far [1,6,7], except for the cell line derived from MeWo melanoma [8].

The DNA- and RNA-binding protein KIN, also known as Kin17, is well conserved among species from lower to higher eukaryotes, suggesting an important role in the maintenance of basic cellular function which remains to be defined [9]. It was identified by